Materials Today Chemistry 45 (2025) 102620

Contents lists available at ScienceDirect

Materials Today Chemistry

journal homepage: www.journals.elsevier.com/materials-today-chemistry/

Lanthanum nickel titanate perovskites as model systems for Ni-perovskite interfacial engineering in methane dry reforming

Thomas F. Winterstein [a], Christoph Malleier [a], Asghar Mohammadi [a], Hannes Krüger [b], Volker Kahlenberg [b], Andrew M. Venter [c], Maged F. Bekheet [d], Julian T. Müller [d], Aleksander Gurlo [d], Marc Heggen [e], Simon Penner [a,*]

[a] Institute of Physical Chemistry, University of Innsbruck, Innrain 52c, A-6020, Innsbruck, Austria
[b] Institute of Mineralogy and Petrography, University of Innsbruck, Innrain 52f, A-6020, Innsbruck, Austria
[c] South African Nuclear Energy Corporation (Necsa), Pretoria, 0001, South Africa
[d] Technische Universität Berlin, Faculty III Process Sciences, Institute of Materials Science and Technology, Chair of Advanced Ceramic Materials, Straße des 17. Juni 135, 10623, Berlin, Germany
[e] Ernst Ruska-Centre for Microscopy and Spectroscopy with Electrons, Forschungszentrum Jülich GmbH, Leo-Brandt-Str. 1, D-52428, Jülich, Germany

ARTICLE INFO

Keywords:
Double perovskite
La_2NiTiO_6
Single perovskite
$La(Ni,Ti)O_3$
Methane
Activation

ABSTRACT

By exploiting the lanthanum – nickel – titanate model system for methane dry reforming (DRM), we show how different (double) perovskite precursor structures can be used to tailor the structure and phase composition of specific Ni – (double) perovskite interfaces by activation in different reducing atmospheres. The key parameter for successful steering of the interface structure is the stability of the parent perovskite material in the respective hydrogen or CO_2–CH_4 mixture. Rietveld refinements of both the precursor perovskite and the interfacial structures verify the sole presence of exsolved Ni and the respective perovskite. Hydrogen reduction of the double perovskite La_2NiTiO_6 leads to exsolution of nm-sized Ni particles and the formation of a Ni–La_2NiTiO_6 interface. Structure refinements based on X-ray and neutron powder diffraction, combined with temperature-programmed hydrogen adsorption, reveal that the prevailing La_2NiTiO_6 is mostly unaffected by the hydrogen treatment and formation of reduced sites is largely suppressed. Treatment of the Ti-doped single perovskite $LaNi_{0.5}Ti_{0.5}O_3$ in a CO_2–CH_4 mixture equally yields Ni exsolution and consequently, a Ni–$LaNi_{0.5}Ti_{0.5}O_3$ interface. Similarly, $LaNi_{0.5}Ti_{0.5}O_3$ is essentially unaffected by the treatment, with interfacial structure and phase composition remaining stable over several DRM cycles. Only hydrogen reduction of $LaNi_{0.5}Ti_{0.5}O_3$ causes complete transformation of the parent perovskite into a Ni–La_2TiO_5/$LaTiO_3$ mixture. All interfaces, including Ni particles impregnated on La_2TiO_5 with outstanding anti-coking behavior, exhibit inherent DRM activity, rivaling or even outperforming undoped $LaNiO_3$. Differences in the stability of (transient) structures during exsolution along the decomposition pathway are mainly due to the Ti dopant, which stabilizes the perovskite structures in reducing atmospheres. This enhanced stability allows us to approach specific Ni-perovskite interfaces and assess their inherent DRM activity.

1. Introduction

Dry reforming of methane (DRM) is a promising reaction to convert the two green house gases CO_2 and CH_4 into syngas, i.e., a hydrogen and carbon monoxide mixture. Depending on the hydrogen/carbon monoxide ratio the latter can be used as feedstock for a variety of synthetic chemicals, including Fischer-Tropsch products, aldehydes, ketones or alcohols. DRM is a highly endothermic reaction and usually needs high reaction temperatures between 600 °C and 1000 °C. A set of parasitic side reactions accompanying the main DRM reaction, including the (reverse) water-gas shift reaction, methane decomposition, water-gas reaction or the Boudouard equilibrium, also occur. The latter is connected to one of the main issues limiting the wide-scale technological use: coking of the catalyst surface by unreactive carbon arising from methane activation. This coking phenomenon is most pronounced in the most widely used catalyst material, metallic Ni. The search for

* Corresponding author.
E-mail address: simon.penner@uibk.ac.at (S. Penner).

https://doi.org/10.1016/j.mtchem.2025.102620
Received 6 December 2024; Received in revised form 6 February 2025; Accepted 1 March 2025
Available online 4 March 2025

alternative catalyst materials and preparation routines with enhanced carbon reactivity has been ongoing for the last decades. A very promising technique which was widely studied in the last few years is metal exsolution from perovskite oxides [1–3].

Perovskites are complex oxides or halogenides with the general formula ABX_3, where A and B are mostly di- and trivalent cations and X is occupied by oxygen or halogen anions (for the A-site, typically earth alkaline and lanthanum are used; the B-site is mostly occupied by transition metal cations) [2]. In contrast, double perovskites are highly ordered structures with the most general formula AA'BB'X_6 [4,5]. While a general advantage of (double) perovskites is the possibility of tuning the physico-chemical properties by adjusting the chemical composition by doping at the respective A- and B-sites and an even finer adjustment of these properties by the use of double perovskites due to the possible accomodation of unusual oxidation states like +6 or +7, a particular benefit is connected to their use as precursor materials. Partial or total decomposition of the perovskites leads to exsolution of metal particles from the perovskite and the associated formation of metal-perovskite or metal-oxide interfaces. Controlled decomposition usually yields interfaces with defined extents. For DRM applications, there is common agreement that the exsolution of Ni from the perovskite host lattice produces better anchored Ni particles with a more extended interface, which enables the bifunctional synergistic action between Ni and perovskite to work more efficiently. In this respect, for $LaNiO_3$, which yields a Ni – La_2O_3 interface after activation, Ni activates CH_4, while the CO_2 activation is provided by a reversible $La_2O_2CO_3$ oxycarbonate formation/decomposition cycle. A specific role for perovskites at a Ni – perovskite interface is the activation of CO_2 at oxygen vacancy sites and the subsequent oxygen spillover to Ni, where it aids in the oxidative removal of carbon deposits [1–3].

One disadvantage of such a steered decomposition is connected to the structural complexity of the perovskites. Even for the archetypical $LaNiO_3$ perovskite in DRM, a sequence of structural transformations occurs: complicated even when the decomposition is performed in hydrogen (involving e.g., the formation of substoichiometric perovskite phases en route to full decomposition), the complexity is significantly enhanced if the decomposition/activation is performed in the DRM mixture directly. Apart from oxygen-deficient perovskite phases, Ruddlesden-Popper phases or lanthanum oxycarbonate phases are also intermediarily observed [6–8]. It is, therefore, imperative to gain fundamental insight into the structure and reactivity of the resulting interfaces to obtain these interfacial structures in a structure- and phase-pure form. Regarding the latter, we note that although such interfaces are reported for hundreds of studies using (doped) perovskites in all sorts of reactions [9], little care is taken in the overwhelming majority of cases to ensure exactly this structure- and phase purity. We use the term "interface" here in a catalytic bifunctional sense to emphasize, that metal and perovskite (or oxide as a result of perovskite decomposition) work together. This may also indicate the simultaneous presence of a physical boundary between two phases, such as Ni-perovskite after Ni exsolution from the perovskite lattice.

To disentangle the specific properties of Ni-perovskite and Ni-double perovskite interfaces in the DRM reaction, we opted for the lanthanum nickel titanium perovskites, as phase- and structure-pure La_2NiTiO_6 and $LaNi_{0.5}Ti_{0.5}O_3$ precursors could be reproducibly prepared by different synthesis strategies. Nickel titanate perovskites have been studied in hydrocarbon dry reforming [3,10,11], methane partial and steam reforming [12,13], carbon dioxide and bi-reforming of methane [12,13] or alcohol steam reforming [14]. In dry reforming, specifically, Ni doping into $Ca_{0.8}Sr_{0.2}TiO_3$ yielded highly active dry reforming materials due to the in situ formation of a Ni-perovskite interface and an easy reverse oxygen spillover to the exsolved Ni particles to assist in oxidative removal of carbon [10]. Sr-doped $La_{0.6}Sr_{0.2}Ti_{0.85}Ni_{0.15}O_3$ perovskites were revealed to benefit from introducing Ti to increase the number of exsolved Ni particles, as well as the catalyst stability. Similarly, the addition of Ti to $La_{0.46}Sr_{0.34}Ti_{0.9}Ni_{0.1}O_3$ caused suppressed coke deposition due to a smaller particle size of metallic Ni produced by the reduction of Ni within the perovskite phase [11].

With the lanthanum nickel titanate system, we are in the prime position to tune the nature of the Ni-perovskite interface by reductive pretreatment/activation and to accordingly highlight the inherent properties and DRM activity of

- the La_2NiTiO_6 structure,
- Ni in contact with La_2NiTiO_6 (through hydrogen reduction),
- Ni in contact with $LaNi_{0.5}Ti_{0.5}O_3$ (through DRM treatment),
- Ni in contact with La_2TiO_5 (through hydrogen reduction of $LaNi_{0.5}Ti_{0.5}O_3$ and exsolution) and
- Ni in contact with La_2TiO_5 (through wet impregnation of La_2TiO_5)

and correlate the reactivity and structural stability to Ti-free $LaNiO_3$ and Ni-free $La_2Ti_2O_7$ benchmark materials of the $LaNiO_3$–$La_2Ti_2O_7$ composition series, as well as pure La_2TiO_5. By a combination of ex situ and in situ spectroscopic and structural characterization (in situ X-ray diffraction, quantitative X-ray analysis, X-ray photoelectron spectroscopy, neutron diffraction, aberration-corrected electron microscopy) and DRM activity, we provide a direct connection between structure and activity of different Ni-perovskite (oxide) interfaces.

2. Experimental

2.1. Synthesis of materials

$LaNi_{0.5}Ti_{0.5}O_3$ was obtained by a modified Pechini method [15] with a metal ion-to-citric acid ratio of 1:2 and a metal ion-to-ethylene glycol ratio of 1:4. Titanium-isopropoxide (Sigma-Aldrich, 97 %) was dissolved in ethylene glycol and stirred at 60 °C for 10 min. Citric acid was subsequently added to the titanium solution before heating the mixture to 90 °C. $La(NO_3)_3{\cdot}6H_2O$ (Carl Roth, 99.99 %) and $Ni(NO_3)_2{\cdot}6H_2O$ (Puratronic, 99.9985 %) were dissolved in water and citric acid. The lanthanum-nickel solution was heated and stirred at 90 °C until all products dissolved, then mixed with the remaining ethylene glycol. Both solutions were combined and stirred at 120 °C–140 °C until a dark brown polymer resin formed. The polymer was calcined in air at 450 °C for 4 h. The resulting ashes were ground to a powder in an agate mortar, sintered at 800 °C for 17 h and ground up again to yield a black homogeneous powder. $LaNiO_3$ and $La_2Ti_2O_7$ were prepared the same way, without nickel nitrate/titanium isopropoxide and adjusting the La/Ni and La/Ti ratio.

La_2NiTiO_6 was obtained by a solid-state synthesis routine [16]. Specifically, stochiometric amounts of La_2O_3 (Sigma-Aldrich, 99.99 %), NiO (Puratronic, 99.998 %) and TiO_2 (Puratronic, 99.5 %) were ground and homogenized in ethanol at 600 rpm for 45 min with an agate ball mill. After drying for 24 h the powder was pressed into 1 g, 0.6 cm diameter pellets with a hydraulic press. The pellets were placed into a platinum crucible and sintered in air for 24 h at 1350 °C. After sintering, the pellets were ground manually in an agate mortar, re-pressed into pellets and sintered for an additional 24 h at 1350 °C. After the second sintering step the pellets were again ground in an agate mortar, yielding a dark green powder. La_2TiO_5 was prepared in a similar way (without Ni). The pellets were subjected to a 48 h air treatmant at 1350 °C.

The Ni–La_2TiO_5 impregnated catalyst was synthesized through a wet impregnation routine. The Ni precursor ($La(NO_3)_3{\cdot}6H_2O$ (Carl Roth, 99.99 %)) was dissolved in water and dropwise added to a suspension of La_2TiO_5 in water under constant stirring. After evaporation of water at 80 °C, the resulting powder was heated for 4 h at 300 °C to yield the calcined NiO– La_2TiO_5 precursor, which was converted to Ni–La_2TiO_5 by subsequent hydrogen reduction at 800 °C for 15 min.

2.2. Ex situ and in situ X-ray diffraction

Ex situ structural analysis of benchmark materials after selected

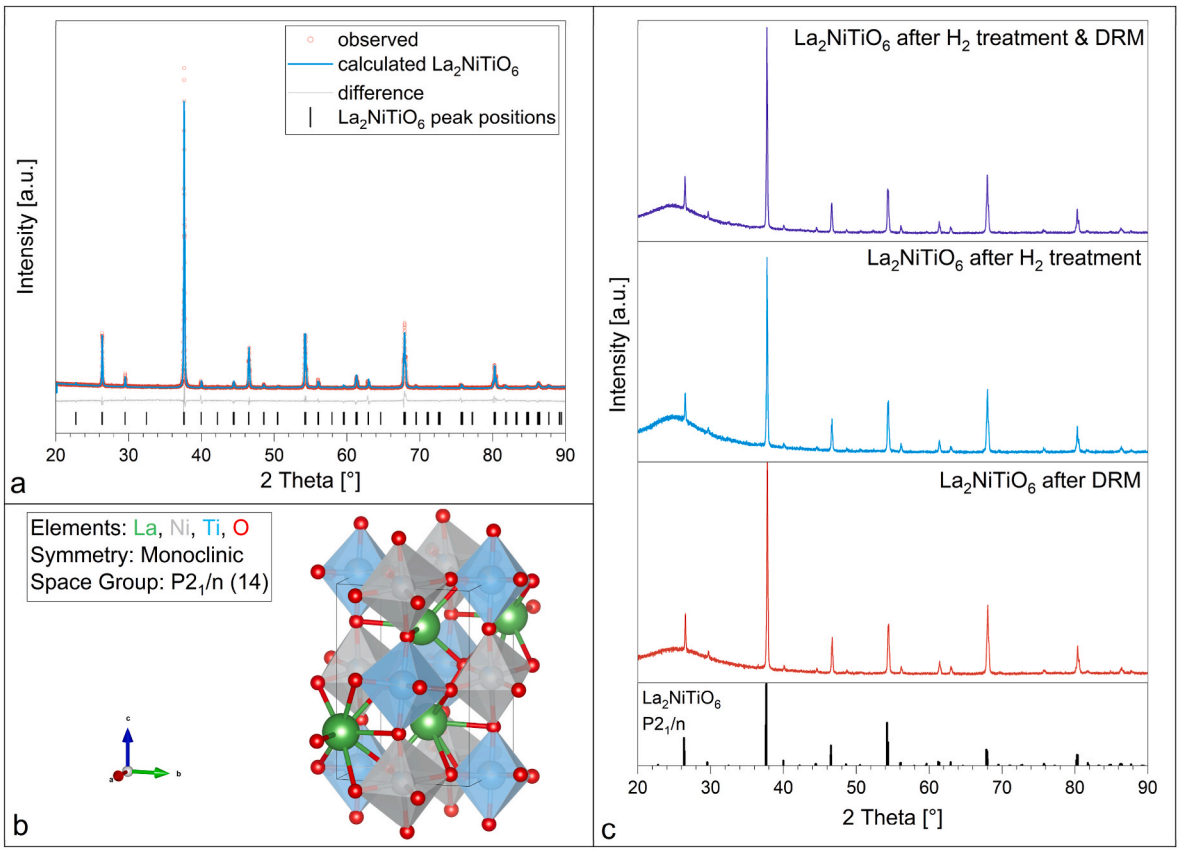

Fig. 1. Panel a: Result of a Rietveld refinement of the calcined La_2NiTiO_6 powder X-ray diffraction pattern. Panel b: VESTA-drawn structure. Panel c: Set of ex-situ collected powder X-ray diffractograms after calcination, after hydrogen reduction at 1000 °C for 2 h, and after a DRM treatment up to 800 °C.

treatments was carried out using a Rigaku SmartLab-SE instrument in Bragg-Brentano geometry (Co-Kα, λ = 1.7890 Å) using a D/teX Ultra 250 compound silicon strip 1D-detector (Rigaku, Tokyo, Japan). The ground sample was placed on a glass-sample holder, and the patterns were recorded in a 2θ range of 5°–90° with a step width of 0.01°.

In situ synchrotron-based PXRD experiments were conducted in both DRM mixtures and under pure hydrogen at beamline 12.2.2, Advanced Light Source (ALS) at Lawrence Berkeley National Laboratory, in a cell previously described in Refs. [17,18]. All diffraction patterns were measured in angle-dispersive transmission mode with a focussed 25 keV monochromatic beam (λ = 0.4984 Å/30 μm spot size). The powders were heated in a 0.7 mm outer diameter quartz capillary under quasi-flowing conditions (CH_4: CO_2 = 1:1, gas flow: 1 mL min^{-1} for DRM; pure hydrogen, gas flow 1 mL min^{-1}, GHSV = 600 000 N mL h^{-1} $gcat^{-1}$). Heating was performed in a SiC furnace with an infrared light source up to 800 °C at a rate of 10 °C min^{-1}. All gases were injected through a 0.5 mm outer diameter tungsten tube [17,18]. The program TOPAS 5.0 by Bruker was utilized to analyze the X-ray diffraction patterns using Rietveld refinement with a full axial model [19]. A Double-Voigt approach was applied to calculate the crystallite sizes. The resolution function of the diffractometers was obtained from the structure refinement of a LaB_6 standard.

2.3. X-ray photoelectron spectroscopy

Surface chemical analysis was carried out in a Thermo Fisher X-ray spectrometer with a Mg/Al dual anode. For all measurements, an Al-K_α X-ray source was used. Perovskite powders were fixed on stainless steel holders using conductive carbon tape. Qualitative analysis was based on the Ni 2p, La 3d, Ti 2p, O 1s and C 1s high-resolution spectra. Chemical shifts were internally calibrated to the La $3d_{5/2}$ component. Fitting of the spectra by different components and oxidation states was performed using literature-reported constraints for the full-width-at-half maximum and the binding energies, where applicable. Background correction was done using Shirley- and Tougaard-type functions.

2.4. Electron microscopy

Scanning and transmission electron microscopy S(T)EM characterization via high-angle annular dark field (HAADF) imaging and Energy-dispersive X-ray analysis was carried out on an C_s-aberration corrected (Ceos DCOR) Hitachi 5000 electron microscope operated at 200 kV at the Ernst Ruska-Centre Jülich. Additional scanning electron microscopy and corresponding energy-dispersive X-ray spectroscopy (EDXS) measurements were performed on a field-free analytical TESCAN Clara ultra-high-resolution scanning electron microscope operated at 10 kV. EDX maps were collected using an Oxford Ultim Max 65 mm^2 detector. Selected samples were coated by a 20 nm Au layer to prevent charging.

2.5. Catalytic and temperature-programmed hydrogen reduction measurements

200 mg of sample powder were placed in a bed of quartz wool inside a 7 mm (inner diameter) quartz tube fixed-bed flow reactor for both H_2 pre-treatments and catalytic measurements. H_2 treatments were conducted in a continuous flow of 20 mL min^{-1} pure H_2 at 1000 °C for 2 h. For catalytic measurements CH_4, CO_2 and He were mixed 1:1:1 with a flow rate of 20 mL min^{-1} each and a heating rate of 5 °C min^{-1} from 50 °C to 800 °C, followed by an isothermal period at 800 °C for 30 min or 90 h for long-term measurements. An external S-type thermocouple was placed in close contact to the reactor tube to ensure correct temperature reading. The output gas was directly detected by an online quadrupole

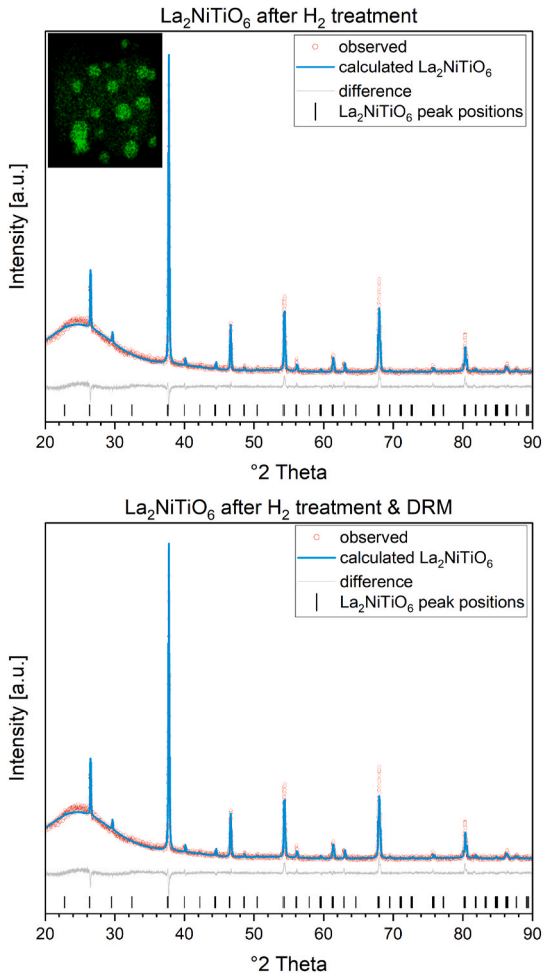

Fig. 2. Results of the Rietveld refinements of the ex-situ collected PXRD patterns of La_2TiNiO_6 after hydrogen reduction for 2 h at 1000 °C (top) and a subsequent DRM experiment up to 800 °C (bottom). The inset shows a Ni EDX map (discussed in Fig. 3) to highlight that local Ni exsolution occurs.

mass spectrometer (Balzers QME 125). CO_2, CH_4, CO, H_2 and He were measured at their respective *m/z* ratios of *m/z* 44, 16, 28, 2 and 4 respectively. Relevant fragmentation patterns were considered. To minimize condensation from potential H_2O formation, silica gel was placed at the reactor output. If a second consecutive DRM cycle was carried out, it was performed in exactly the same way as the associated first cycle.

For display of the catalytic data, we show the conversion of the relevant signals as a qualitative measure of the catalytic activity, as due to the ongoing structural transformations during the DRM reaction, active-site-normalized reaction rates and consequently, turnover frequency (TOF) values cannot be reliably calculated.

Hydrogen temperature-programmed reduction (H_2-TPR) and temperature-programmed desorption (TPD) measurements were performed in a setup for volumetric adsorption of gases consisting of a quartz tubular reactor (V = 36 mL). H_2-TPR is conducted under static conditions. As for H_2-TPR, a defined amount of about 70 mg of the powder sample was fixed by quartz wool in the reactor in a chemically inert environment. Catalysts are pretreated in flowing dry O_2 for 1 h at 700 °C and subsequently cooled down in O_2 atmosphere. In order to desorb surface- and physically-adsorbed oxygen, samples are evacuated up to a defined base pressure of 10^{-6} mbar. During H_2-TPR, a defined (ca. 490 mbar) amount of pre-dried H_2 (using a liquid N_2 cooling trap) was expanded from a separately calibrated volume (9 mL) into the entire reactor volume. A zeolite trap is installed after the reactor to remove reaction-formed water. After equilibration of the final reactor pressure, the temperature program was started to measure the H_2 uptake up to 900 °C. The temperature program included a heating phase from 25 °C to 900 °C at a rate of 10 °C min^{-1}, followed by an isothermal period at 900 °C for 10 min, and finally, a cooling process to room temperature (rate 10 °C min^{-1}). Additional information, including the technical information of the setup, test conditions, and method of calculation of the H_2-uptake, is provided in Refs. [20,21] A QMS system from Balzers (QMA 125; QME 125-9) was employed for continuous gas analysis during TPD measurements. Relevant gases were detected by their respective molecular ions: H_2 (*m/z* 2), H_2O (*m/z* 17/18), CO (*m/z* 28), O_2 (*m/z* 32), CO_2 (*m/z* 44). After the H_2-TPR phase, the samples are evacuated at 25 °C to 10^{-6} mbar and subsequently, heating was started with the same temperature program as for the H_2-TPR tests. The only dominant desorbed species in all TPD tests was H_2. The H_2 MS signal was calibrated via a separate effusion experiment, where H_2 was pumped from the reactor (without sample) via a capillary leak into the QMS chamber. This way, the effusion rate – calculated from absolute pressure decrease vs. time in the reactor chamber – was obtained in [mol s^{-1}] and correlated to the respective H_2 MS signal. Based on this calibration function, the H_2 desorption rates were calculated from the TPD MS signal.

2.6. Neutron powder diffraction measurements

The neutron powder diffraction patterns were collected on the PITSI instrument [22] at the SAFARI-1 research reactor. The powdered samples filled approximately 60 % of the available volume in thin-walled vanadium tubes, 5 mm in diameter by 50 mm in height. Samples, fully bathed in the monochromatic neutron beam of wavelength 1.76 Å, were continuously rotated during the investigations to homogenise the grains. The data were normalized against a beam monitor counter to negate variations in the reactor power level, as well as corrections applied for detector efficiency. Rietveld analysis on the thermal neutron powder diffraction (NPD) data acquired at a wavelength of 1.76 Å was conducted with the program TOPAS version 6.0 [23]. Chebyshev polynomials with twelve coefficients were used to describe the background, and a modified Thompson-Cox-Hastings pseudo-Voigt function including an asymmetry correction was selected to model the peak profiles.

2.7. Brunauer-Emmett-Teller (BET) measurements of the specific surface area

BET specific surface areas were measured on a Micromeritics 3Flex ChemBET apparatus using krypton as adsorbent at −196 °C. All samples were degassed under vacuum at 200 °C for 1 h. Specific surface areas (SSA's) of 6.8547 m^2g^{-1} for $LaNi_{0.5}Ti_{0.5}O_3$ and 0.4629 m^2g^{-1} for La_2NiTiO_6 have been determined. The respective BET surface area plots are shown in Section A of the SI (Figs. S1 and S2).

3. Results and discussion

3.1. Tuning the interface structure by using different La–Ti–Ni precursor structures

3.1.1. Partial Ni exsolution from La_2NiTiO_6 during hydrogen reduction or DRM: the Ni – La_2NiTiO_6 interface

Fig. 1 shows a combination of ex situ X-ray diffractograms after selected treatments alongside Rietveld refinement of the diffractogram of the calcined sample and a VESTA [24]-visualized double perovskite structure. La_2NiTiO_6 crystallizes in the monoclinic space group $P2_1/n$ and the X-ray diffraction pattern of the calcined sample (Panel a) can be fitted with La_2NiTiO_6 phase from Ref. [23] without any parasitic side phases. The structure model (Panel b) illustrates the larger perovskite unit cell resulting from the ordering along the c axis. To test the stability

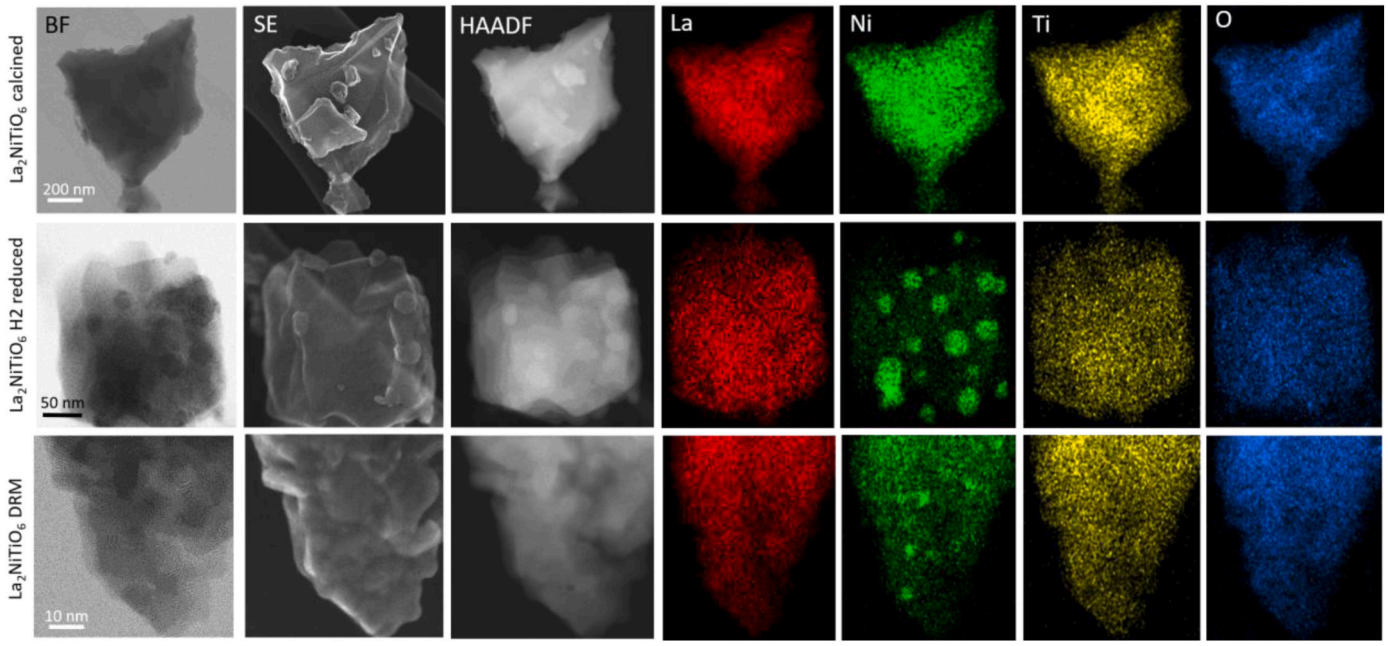

Fig. 3. Electron microscopy analysis of La_2NiTiO_6 in the calcined state (top row), after hydrogen reduction for 2 h at 1000 °C (middle row) and after treatment in the DRM mixture at 800 °C for 30 min. Bright-field (BF), secondary electron (SE), and HAADF STEM images are shown in separate columns for each treatment. In addition, chemical analysis by EDX based on the La–K (red), Ni–K (green), Ti–K (yellow) and O–K (blue) edges is also presented in individual panels.

Table 1
Weight fraction analysis, lattice parameters and crystallite sizes observed on La_2NiTiO_6 and $LaNi_{0.5}Ti_{0.5}O_3$ after selected hydrogen and DRM treatments. Numbers in column 3 refer to the weight percentages of the phases obtained from a quantitative phase analysis (QPA) based on the Rietveld refinements. According to our experience, the accuracy of the QPA results is estimated to be 1–2 wt.-%. In any way, the errors are significantly higher than those obtained from the Rietveld analysis software reflecting only the mathematical fit between measured and calculated step intensities.

Sample	Phase	Weight Fraction [wt.%]	Lattice Parameters [Å] a b c			CrySize [nm]
La_2NiTiO_6 a.c.	La_2NiTiO_6	100	5.56	5.55	7.85	–
La_2NiTiO_6 DRM	La_2NiTiO_6	100	5.56	5.55	7.85	–
La_2NiTiO_6 H_2	La_2NiTiO_6	100	5.57	5.55	7.85	–
La_2NiTiO_6 H_2+DRM	La_2NiTiO_6	100	5.57	5.55	7.85	–
$LaNi_{0.5}Ti_{0.5}O_3$ a.c.	$LaNi_{0.5}Ti_{0.5}O_3$	100	5.56	–	13.55	30
$LaNi_{0.5}Ti_{0.5}O_3$DRM	$LaNi_{0.5}Ti_{0.5}O_3$	96	5.56	–	13.57	30
	Ni	4	3.53	–	–	20
$LaNi_{0.5}Ti_{0.5}O_3$ DRMx2	$LaNi_{0.5}Ti_{0.5}O_3$	93	5.56	–	13.57	30
	Ni	7	3.53	–	–	15
$LaNi_{0.5}Ti_{0.5}O_3$ H_2	La_2TiO_5	57	11.00	3.95	11.37	70
	$LaTiO_3$	27	5.56	5.57	7.86	30
	Ni	15	3.53	–	–	30
	La_2NiO_4	1	5.47	5.47	12.77	80
$LaNi_{0.5}Ti_{0.5}O_3$ H_2+DRM	La_2TiO_5	56	10.99	3.95	11.37	70
	$LaTiO_3$	25	5.56	5.58	7.86	30
	Ni	15	3.53	–	–	30
	La_2NiO_4	4	5.46	5.54	12.72	30
$LaNi_{0.5}Ti_{0.5}O_3$ H_2+DRM	La_2TiO_5	72	11.00	3.95	11.39	80
90h	$LaTiO_3$	2	5.61	5.59	7.79	50
	Ni	13	3.53	–	–	40
	La_2NiO_4	2	5.48	5.47	12.79	70
	Graphite	11	2.46	–	6.83	10

Table 2
Rietveld refined crystallographic parameters for the three samples of monoclinic La_2NiTiO_6 (space group: $P2_1/n$) treated under different experimental conditions as derived from the neutron diffraction data shown in Fig. S4.

	a **[Å]**	***b*** **[Å]**	***c*** **[Å]**	**β [°]**	**V [Å^3]**
Untreated	5.5244(9)	5.5418(8)	7.8138(15)	90.080(16)	239.22(7)
H_2-treated	5.5310(7)	5.5399(4)	7.8195(8)	90.007(14)	239.60(4)
DRM-treated	5.5253(6)	5.5426(4)	7.8113(11)	90.129(10)	239.22(5)

of La_2NiTiO_6 under reduction and DRM conditions, Panel c highlights the respective PXRD patterns after selected treatments, respectively. Neither hydrogen reduction at 1000 °C for 2 h nor multiple DRM treatments up to 800 °C (also in combination with hydrogen pre-treatments) show any sign of crystalline decomposition products or exsolved Ni. This is also confirmed by the Rietveld-fitted X-ray diffractograms after hydrogen reduction and a subsequent DRM treatment (Fig. 2). Table 1 summarizes the lattice parameters and weight fractions of the detected phases after selected treatments.

We have further examined La_2NiTiO_6 by synchrotron-based in situ XRD investigations during hydrogen reduction and DRM treatments

Table 3
Atomic coordinates and site occupancies for monoclinic La_2TiNiO_6 as derived from the neutron diffraction data shown in Fig. S4. First line: Untreated; second line: H_2-treated; third line: DRM-treated.

Atom	Wyckoff-site	x	y	z	Occupancy	B_{iso} [Å^2]
La	4*e*	0.505 (2)	0.535 (1)	0.252(1)	1.0	1.01(3)
		0.496 (3)	0.529 (1)	0.250(1)	1.0	1.01
		0.500 (1)	0.530 (1)	0.244(1)	1.0	1.01
Ti1	2*d*	0.5	0	0	0.46(1)	1.61(3)
					0.48(1)	1.61
					0.46(1)	1.61
Ni1	2*d*	0.5	0	0	0.54(1)	1.61(3)
					0.52(1)	1.61
					0.54(1)	1.61
Ti2	2*c*	0	0.5	0	0.54(1)	1.61(3)
					0.52(1)	1.61
					0.54(1)	1.61
Ni2	2*c*	0	0.5	0	0.46(1)	1.61(3)
					0.48(1)	1.61
					0.46(1)	1.61
O1	4*e*	0.217 (2)	0.222 (4)	−0.033 (2)	1.0	0.62(1)
		0.221 (2)	0.213 (4)	−0.035 (2)	1.0	0.62
		0.232 (2)	0.213 (2)	−0.032 (2)	1.0	0.62
O2	4*e*	0.277 (3)	0.712 (4)	−0.042 (2)	1.0	0.62(1)
		0.279 (2)	0.716 (4)	−0.037 (2)	1.0	0.62
		0.288 (2)	0.711 (2)	−0.040 (1)	1.0	0.62
O3	4*e*	0.428 (3)	0.988 (2)	0.245(2)	1.0	0.62(1)
		0.422 (2)	0.984 (2)	0.250(1)	1.0	0.62
		0.423 (2)	0.989 (1)	0.236(2)	1.0	0.62

(Fig. S3). Corroborating the ex situ data, no crystalline phase or structural changes were detected (for some diffractograms, additional peaks of the SiC furnace material are present).

To test the stability of reactive lattice oxygen and to validate the occupancy on the B/B' site, we performed neutron diffraction experiments. In comparison to X-rays, neutrons allow for more precise differentiation between Ni and Ti (coherent scattering lenghts: b_{Ni}: 10.3 fm, b_{Ti}: −3.44 fm [25,26]). Moreover, the coherent scattering length of oxygen is more similar to that of the metals (b_O: 5.80 fm). The initial atomic coordinates and site occupancies for La_2TiNiO_6 were taken from the work of Rodriguez et al. [24] The total distribution of the Ti and Ni ions on the positions 2d and 2c, respectively, was constrained to the expected stoichiometric ratio of 1:1. The resulting lattice parameters are presented in Table 2. The relevant refinement residuals for the three samples are as follows: R_{wp} = 3.44 %, R_{Bragg} = 0.77 %, GoF = 2.02 (untreated); R_{wp} = 4.20 %, R_{Bragg} = 2.86 %, GoF = 1.58 (H_2-treated); R_{wp} = 4.21 %, R_{Bragg} = 0.91 %, GoF = 1.55 (DRM-treated).

Refinement of the site occupancies of the oxygen atoms did not yield clear indications of the presence of reduced sites as the site populations were found to be equal to 1.0 within two standard uncertainties. In the case of the H_2-treated material, for example, the corresponding values were 0.99(3) (for O1), 0.97(3) (for O2) and 1.02(3) for (O3). Furthermore, the refinement calculations also indicated that the La site is fully occupied. Note, that the Ti/Ni distributions on the two different octahedral sites are more similar when compared with the results obtained by Rodriguez et al. for their samples [25]. The results of the final structure refinements are summarized in Table 3.

Both X-ray and neutron diffraction showed no crystalline parasitic phases after any treatment. Rietveld refinement of the oxygen occupancy in the neutron data for La_2TiNiO_6 especially rule out a significant contribution of reduction-induced reduced sites. To check, if isolated X-ray invisible local Ni particle exsolution occurs, electron microscopy analysis was performed after selected treatments (Fig. 3). In the calcined state, large aggregates of several hundred nm are observed, which appear as monolithic blocks in the secondary electron (SE) contrast. This confirms the low specific surface area arising from the very high synthesis temperatures. Chemically, the sample appears very bulk-homogeneous. This chemical homogeneity is lifted after hydrogen reduction at 1000 °C for 2 h, and to a lesser extent, also after DRM. In both cases, Ni exsolution indeed occurs locally. After hydrogen reduction, the Ni particle size is larger (20 nm–50 nm) and Ni exsolution occurs more frequently. In contrast, after DRM, the Ni particles are significantly smaller in size (sub-20 nm) and more Ni remains in the double perovskite structure. The distribution of La, Ti and O still remains homogeneous. Combining both diffraction and electron microscopy analysis, we infer that a Ni–La_2NiTiO_6 interface is present after either treatment.

3.1.2. *Partial Ni exsolution from $LaNi_{0.5}Ti_{0.5}O_3$ during DRM: the Ni – $LaNi_{0.5}Ti_{0.5}O_3$ interface*

To provide corresponding structural data on a phase-pure single Ni-perovskite interface, we studied a Ti-doped $LaNiO_3$ sample with a nominal Ti/Ni ratio of unity, i.e., a composition of $LaNi_{0.5}Ti_{0.5}O_3$ under similar experimental conditions as the double perovskite (with respect to hydrogen reduction and DRM tests). The Rietveld-refined PXRD pattern of Fig. 4, Panel a indicates the presence of phase-pure trigonal $LaNi_{0.5}Ti_{0.5}O_3$ in accordance with ref. [27]. The PXRD pattern after a DRM treatment without prior hydrogen reduction (red pattern in Panel b, Rietveld-fitted diffractogram in Fig. 5) shows that Ni exsolution in a carbon-dioxide/methane mixture indeed leads to an exsolved Ni amount of ca. 4 wt.-% (cf. Table 1). A second DRM cycle (purple pattern) increases the amount of exsolved Ni to about 7 wt.-%. However, the structure of the parent $LaNi_{0.5}Ti_{0.5}O_3$ material remains largely unaffected by the treatments. This is also confirmed by the Rietveld refinement of the diffractograms after one and two DRM cycles (Fig. 5). We, therefore, infer the exclusive presence of a structurally stable Ni–$LaNi_{0.5}Ti_{0.5}O_3$ interface (for the sake of clarity, we still refer to "$LaNi_{0.5}Ti_{0.5}O_3$", despite Ni exsolution). Ni exsolution can also be seen in the electron microscopy images and the respective EDX maps (Fig. 6). Ni particles appear well-distributed on the surface of $LaNi_{0.5}Ti_{0.5}O_3$ with average particle sizes of around 20 nm–50 nm. The maps also show that the majority of Ni still remains within the perovskite lattice. Local EDX measurements also confirm that exclusive Ni exsolution occurs, ruling out exsolved Ni–Ti alloy particles.

3.1.3. *Full decomposition of $LaNi_{0.5}Ti_{0.5}O_3$ in hydrogen: Ni in contact with La_2TiO_5 and $LaTiO_3$ phases*

To test the stability of $LaNi_{0.5}Ti_{0.5}O_3$ and to force Ni exsolution to a higher degree, we performed hydrogen reduction prior to the DRM treatments. The purple pattern in Fig. 4c indicates total decomposition of $LaNi_{0.5}Ti_{0.5}O_3$ into a mixture of different La–Ni and La–Ti perovskite phases aside from Ni. The main crystalline phase (~56 wt.-%) is orthorhombic La_2TiO_5 (space group *Pnma*) followed by cubic $LaTiO_3$ (space group *Pm-3m*) at 25 wt.-%. The Ruddlesden-Popper phase La_2NiO_4 (tetragonal, space group *I4/mmm*) is also present at 4 wt-%, alongside ca. 15 wt.-% Ni. Especially La_2TiO_5 is a common reaction product of La–Ti perovskite decomposition under hydrogen reduction, as reported by Tuza et al. using La_2NiTiO_6 [32] and Arrive et al. on $La_{0.5}Sr_{0.5}Ti_{0.75}Ni_{0.25}O_3$ [33]. With respect to the appearance of La_2NiO_4 during hydrogen reduction, interestingly, the effect of Ti is to stabilize La_2NiO_4, as it is not observed on pure $LaNiO_3$ after hydrogen reduction [5]. As indicated by the magenta-colored diffractogram in Fig. 4c, a subsequent DRM treatment does not alter the composition of the structural product mixture, and specifically, no crystalline phases

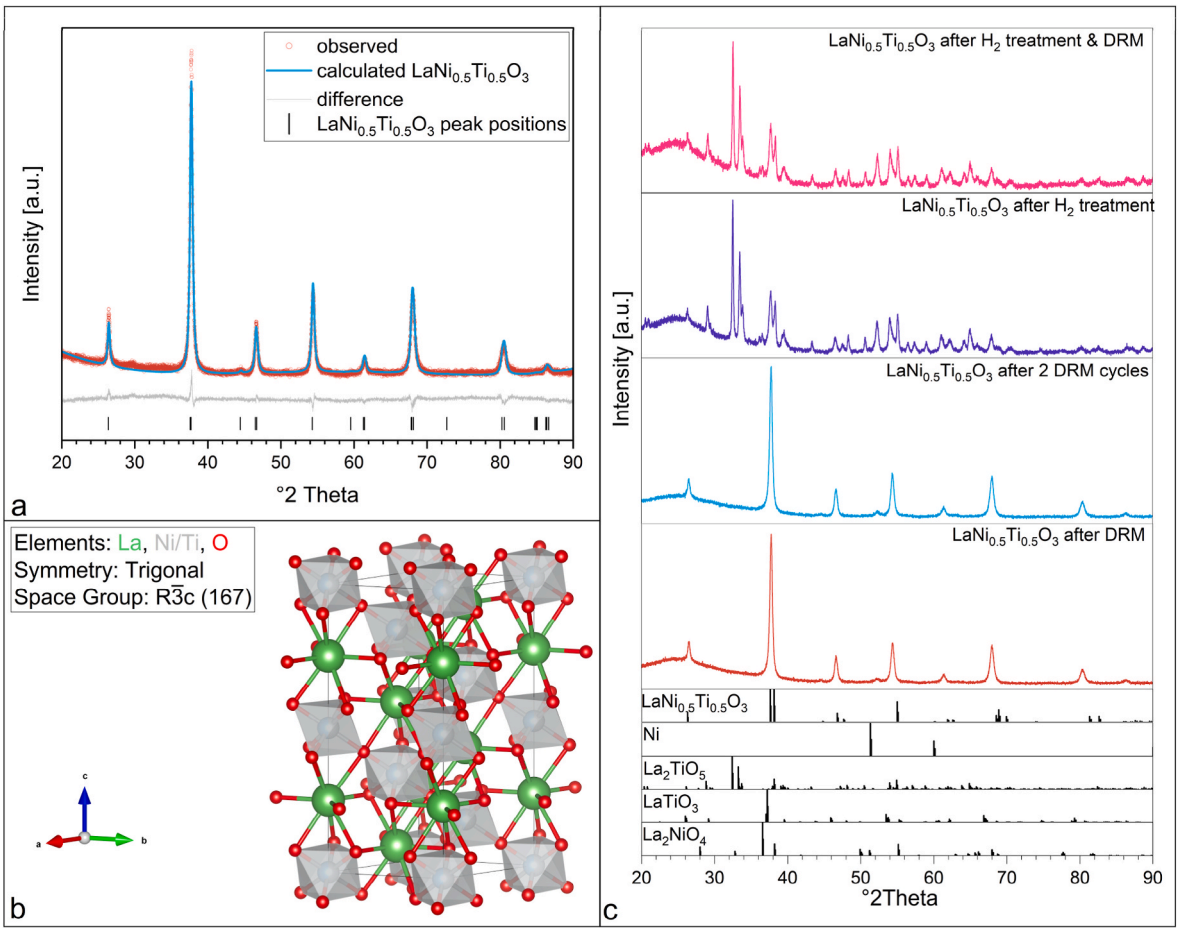

Fig. 4. Panel a: Results of the Rietveld refinement of the powder X-ray diffraction of calcined $LaNi_{0.5}Ti_{0.5}O_3$. Panel b: VESTA-drawn structure. Panel c: Set of ex-situ collected powder X-ray diffractograms after calcination, after hydrogen reduction at 1000 °C for 2 h, after one and two cycles of DRM treatment without hydrogen pre-reduction and after a hydrogen prereduction-DRM cycle. Reference diffractograms: Ni [28], La_2TiO_5 [29], $LaTiO_3$ [30], La_2NiO_4 [31].

related to CO_2 or CH_4 activation are observed. Also in this respect, the introduction of Ti leads to a different pathway of phase formation compared to $LaNiO_3$ [5]. Particularly striking is the absence of lanthanum oxycarbonate phases.

The exsolution of Ni particles can also be directly seen in the electron microscopy images (Fig. 7). Again, no concurrent Ti exsolution is observed, although the exsolved Ni particles are much larger in size (50 nm–100 nm) compared to both simple DRM treatment of $LaNi_{0.5}Ti_{0.5}O_3$ and hydrogen treatment of La_2TiNiO_6. We tentatively explain this by the suppressed anchoring of the Ni particles to the parent perovskite phases because of total $LaNi_{0.5}Ti_{0.5}O_3$ decomposition. In essence, the catalyst after full decomposition resembles a Ni-impregnated $La_2TiO_5/LaTiO_3$ catalyst.

3.2. *Testing the redox properties of Ni perovskite materials by H_2-temperature-programmed reduction (TPR)*

Since metallic Ni nanocrystallites exsolved from the perovskite structure in either hydrogen or DRM mixture in contact with reduced perovskite are supposedly the active species for the reaction, the reducibility as a key parameter of the exsolution process was tested in static H_2-TPR experiments. In addition, as there is a possibility of minor hydrogen dissolution into the perovskite structure during H_2-TPR [21], and in order to quantify the amount of real reduced sites during H_2-TPR more carefully, subsequent TPD yields the integral H_2 desorption. During TPD, dissolved hydrogen can be desorbed in the form of molecular H_2 or water. The following experimental sequence was used in these calculations.

Step 1 H_2-TPR: integral H_2 uptake = reduced sites formed during TPR + dissolved hydrogen

Step 2 TPD: bound hydrogen = desorbed H_2 + desorbed H_2O (reduced sites formed during subsequent TPD).

It should be noted that the additional reduction during TPD with respect to H_2O desorption is not significant [21]. Therefore, in order to prevent the sample from being exposed to air after the H_2-TPR test, the zeolite used during H_2-TPR was not removed from the reactor chamber for the subsequent TPD step (i.e., all desorbed water during TPD was excluded from QMS detection). To a reasonable approximation, the amount of reduced sites during TPR can be calculated as follows:

$$\textit{Number of reduced sites}\ (TPR) = H_{2,int}(TPR) - H_{2,des}(TPD)$$

$H_{2,int}(TPR)$… integral H_2 uptake during TPR

$H_{2,des}(TPD)$… integral H_2 desorbed during TPD

Fig. 8 shows the integral H_2 uptake profiles on $LaNiO_3$, $LaNi_{0.5}Ti_{0.5}O_3$ and La_2NiTiO_6 during temperature-programmed H_2 reduction up to 900 °C. The H_2 uptake profiles during the isothermal phase (10 min), as well as during cooling to 25 °C, are shown as dashed lines for each catalyst. To highlight the H_2 consumption onset temperatures and peaks during heating, the temperature-dependent first derivative of the integral H_2 uptake, i.e., the uptake rate, is additionally shown in Fig. S5. The onset temperatures for major H_2 consumption are 80 °C, 145 °C and 260 °C for $LaNiO_3$, $LaNi_{0.5}Ti_{0.5}O_3$ and La_2NiTiO_6, respectively. According to Fig. 8, for $LaNiO_3$ all hydrogen in the reactor is consumed at temperatures below 500 °C. Therefore, the reduction process, in fact

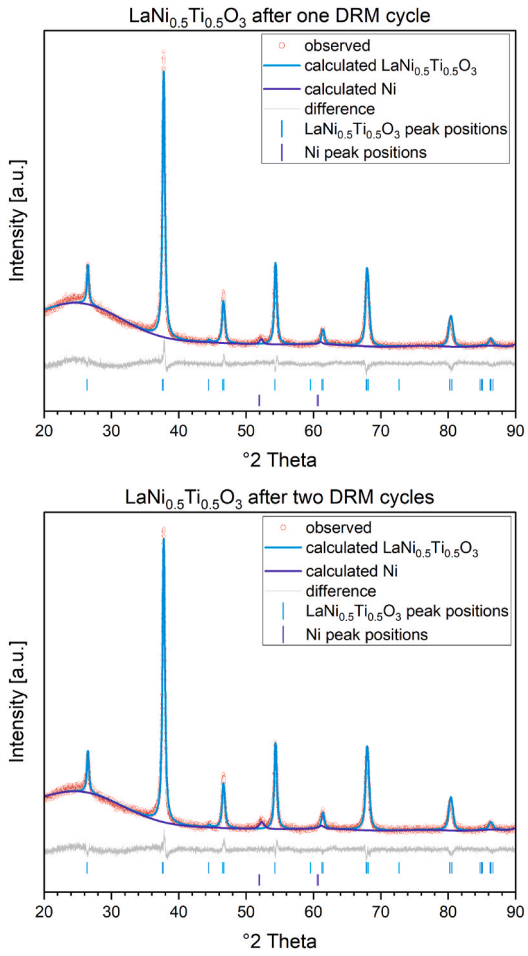

Fig. 5. Results of the Rietveld refinements of the ex situ collected PXRD patterns of $LaNi_{0.5}Ti_{0.5}O_3$ after one (top) and two (bottom) DRM experiments up to 800 °C.

stops during further heating to 900 °C. Considering also Fig. S5, for $LaNiO_3$ the uptake rate peaks at 360 °C and decreases above a shoulder at 410 °C. The latter could be due to effects of hydrogen diffusion limitation [20]. This hypothesis is reasonable due to the delayed processes of bulk reduction compared to that of surface regions. The maximum of the main reduction peak at 360 °C in our study corresponds very well with literature [34–39]. Although there is a general agreement in literature regarding the order of reduction in the oxidation state of Ni ($Ni^{3+} \rightarrow Ni^{2+} \rightarrow Ni^0$) starting from $LaNiO_3$, in the presence of H_2, there is an apparent contradiction with respect to the appearance of transient reduced phases. Intermediate formation of $La_2Ni_2O_5$, NiO, La_2NiO_4 and $La_4Ni_3O_{10}$ phases have been reported at different reduction temperatures [35,37–40]. However, according to our previous work on the structural dynamics of the rhombohedral $LaNiO_3$ catalyst upon in situ reduction in flowing hydrogen up to 800 °C, polymorphic changes to cubic $LaNiO_3$, triclinic $LaNiO_{2.7}$ and monoclinic $LaNiO_{2.5}$ and finally, decomposition into metallic Ni and hexagonal La_2O_3 phases have been observed [6]. The appearance of different phases is strongly dependent on the experimental conditions and if the reduction process is monitored in situ.

The total amount of hydrogen required for the complete reduction of the perovskite according to the following stoichiometry, is equal to $6.108 \cdot 10^{-3}$ mol g^{-1}.

$$2LaNiO_3\ (s) \rightarrow La_2O_3\ (s) + 2Ni\ (s) + 3O\ (g)\ (\text{corresponding to } 1.5O_2)$$

By comparing this value with the total number of created reduced sites on $LaNiO_3$ during TPR, $2.75 \cdot 10^{-3}$ mol g^{-1} (calculated using the integral H_2 uptake during TPR, $2.80 \cdot 10^{-3}$ mol g^{-1} and the integral H_2 desorption during TPD, $0.53 \cdot 10^{-4}$ mol g^{-1}; see Table 4 and Fig. 8), it can be concluded that the catalyst does not get fully reduced under these experimental conditions, which is in good agreement with the ex-situ XRD results after H_2-TPR/TPD (Fig. S7) showing Ni/NiO in contact with La_2NiO_4. We emphasize again that the integrally consumed amount od H_2 on $LaNiO_3$, $2.80 \cdot 10^{-3}$ mol g^{-1}, corresponds to all hydrogen used for the test.

According to Fig. 8 and Table 4, addition of Ti to the perovskite structure leads to a considerable improvement in stability (cf. PXRD pattern in Fig. S7 indicating that $LaNi_{0.5}Ti_{0.5}O_3$ is still largely stable despite static hydrogen treatment) because, in addition to kinetically delayed hydrogen consumption, there are also a significant difference in the integral amount of hydrogen consumed during the test. The differences are even much more pronounced in the case of $La_2NiTiO_{6-\delta}$. In addition to the fact that nanostructures, such as crystallite size, can have a significant effect on the redox properties of metal oxides [41,42], the presence of reducible elements at different positions of the crystal structure, as well as the neighboring chemical composition, also have a significant effect on reducibility. For example, in the case of supported Ni on alumina, the reduction of Ni^{2+} to Ni^0 occurs at 496 °C and 843 °C, which is attributed to Ni^{2+} ions incorporated into tetrahedral and octahedral vacancies, respectively [43,44]. According to Fig. S5 the reduction peaks below 500 °C appear for all three catalysts in almost the same temperature range with different intensities. The broad peaks observed for the two catalysts with Ti in temperature ranges higher than 600 °C could be due to the formation of metallic nickel particles (which is already delayed compared to $LaNiO_3$), subsequently increasing the

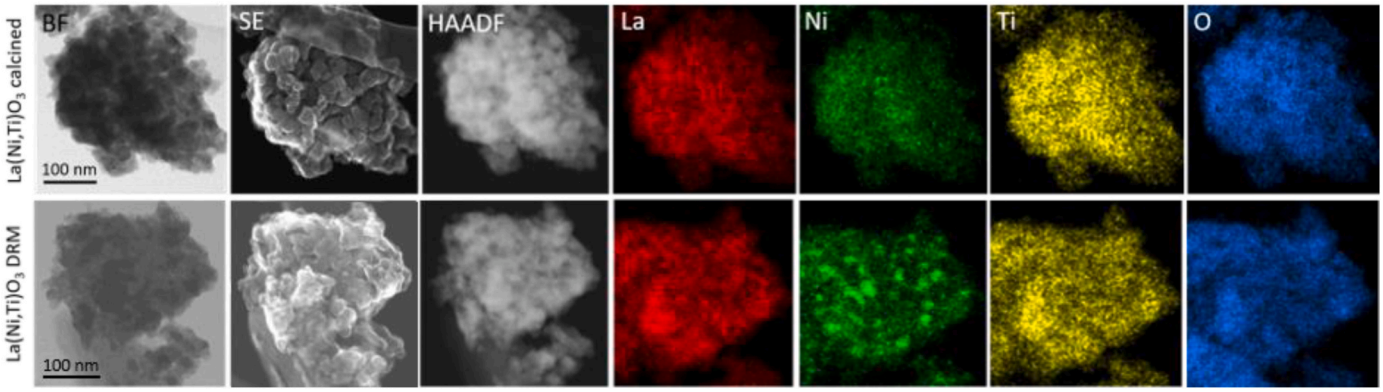

Fig. 6. Electron microscopy analysis of $LaNi_{0.5}Ti_{0.5}O_3$ in the calcined state (top row), and after a treatment in the DRM mixture at 800 °C for 30 min (bottom row). Bright-field (BF), secondary electron (SE), and HAADF-STEM images are shown in separate columns for each treatment. In addition, chemical analysis by EDX based on the La–K (red), Ni–K (green), Ti–K (yellow) and O–K (blue) edges is also presented in individual panels.

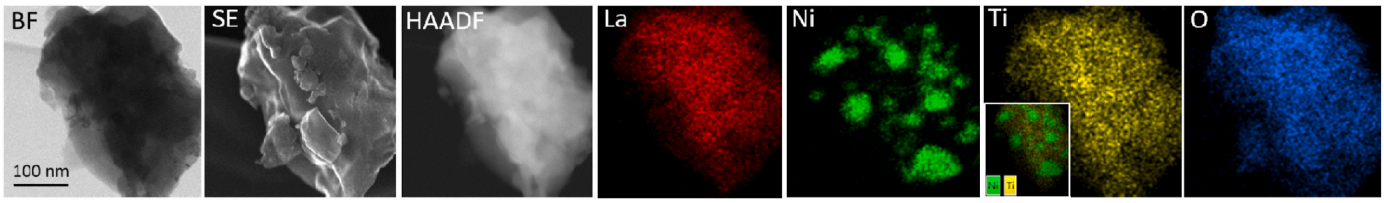

Fig. 7. Electron microscopy analysis of $LaNi_{0.5}Ti_{0.5}O_3$ after hydrogen reduction for 2 h at 1000 °C (middle row). Bright-field (BF), secondary electron (SE), and HAADF STEM images are shown in separate columns for each treatment. In addition, chemical analysis by EDX based on the La–K (red), Ni–K (green), Ti–K (yellow) and O–K (blue) edges is also presented in individual panels.

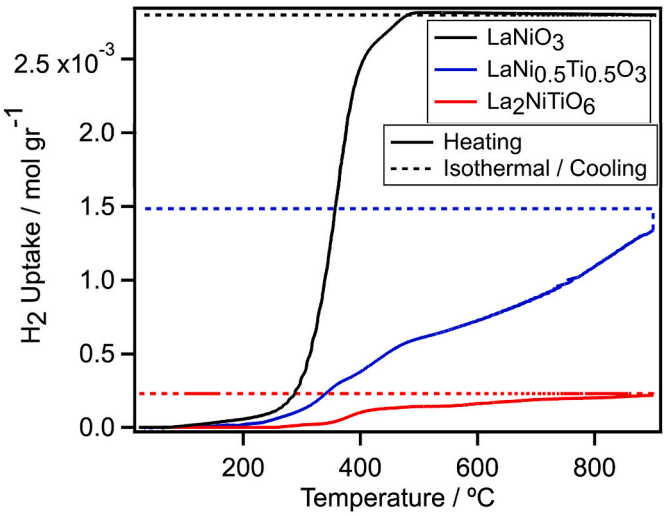

Fig. 8. Integral H_2 uptake during static temperature-programmed H_2 reduction on $LaNiO_3$, $LaNi_{0.5}Ti_{0.5}O_3$ and La_2NiTiO_6 catalysts, after pre-oxidation in flowing O_2 using an initial H_2 pressure of 125 mbar. Temperature program: heating from 25 °C to 900 °C (10 °C min^{-1}/full lines), followed by an isothermal period at the maximum temperature (900 °C for 10 min/broken line) and a cooling phase (10 °C min^{-1}/broken line).

Table 4
Amounts of the integral H_2 uptake, bound hydrogen (H_2 desorption) and created oxygen vacancy during TPR.

Sample	Integral H_2 uptake in TPR /mol g^{-1}	Integral H_2 desorption in TPD /mol g^{-1}	Number of reduced sites (TPR) /mol g^{-1}
$LaNiO_{3-\delta}$	$2.80 \cdot 10^{-3}$	$0.53 \cdot 10^{-4}$	$2.75 \cdot 10^{-3}$
$LaNi_{0.5}Ti_{0.5}O_{3-\delta}$	$1.50 \cdot 10^{-3}$	$2.74 \cdot 10^{-4}$	$1.23 \cdot 10^{-3}$
$La_2NiTiO_{6-\delta}$	$2.30 \cdot 10^{-4}$	$0.38 \cdot 10^{-4}$	$1.92 \cdot 10^{-4}$

oxide reducibility. Taking into account also the crystallite size differences of the samples (Table 1), significant differences in the redox properties of the samples are not surprising. Accordingly, we have shown that increasing the crystallite size of copper-manganite perovskites leads to a pronounced decrease in their reducibility [42].

The H_2-TPD spectra collected from all three samples after H_2-TPR (Table 4 and Fig. S6) show that a small amount of the total hydrogen consumed in the reduction stage is dissolved within the perovskite structure. However, Fig. S6 represents two distinct and well-separated desorption rate maxima, which might indicate a certain difference with respect to the binding energies of hydrogen species on all studied samples [21]. Corroborating the XRD and neutron diffraction experiments, the low amount of desorbed hydrogen for La_2NiTiO_6 compared to $LaNi_{0.5}Ti_{0.5}O_3$ is again evident. At this stage, the question arises how the hydrogen consumption is connected to the Ni exsolution on La_2NiTiO_6. Table 4 and Fig. 8 directly prove, that Ni exsolution goes along with a very minor hydrogen uptake. Therefore, we can safely assume that oxygen vacancy formation (and accordingly the appearance of reaction-formed water) occurs in parallel to Ni exsolution to some extent – however, still within the error margin of the oxygen occupancy determination by neutron diffraction discussed in section 3.1.

3.3. Surface-chemical consequences of Ni-lanthanum nickel titanate interfacial engineering

The surface-related redox chemical state of the different Ni-perovskite interfaces was examined by ex situ XP studies on $LaNi_{0.5}Ti_{0.5}O_3$ after selected treatments necessary to induce the formation of the respective interfaces. The corresponding studies have also been performed on La_2NiTiO_6, but due to the high surface- and bulk structural stability, no changes were observed after any of the treatments (corroborating the XRD and neutron diffraction experiments, as well as the hydrogen uptake results). We provide only data on the Ti 2p, O 1s and C 1s spectra, as due to the strong overlap of the La 3d and Ni 2p peaks [45], the latter are not interpretable. If the Ti 2p and O 1s spectra in Fig. 9 after selected treatments are compared, we note that the as-calcined sample exhibits a single Ti^{4+} 2p component with two peaks at 458.8 eV and 464.5 eV, corresponding to Ti^{4+} $2p_{3/2}$ and Ti^{4+} $2p_{1/2}$, respectively [46–50]. This implies, that in contrast to pure $LaNiO_3$, where all Ni is in the oxidation state Ni^{3+}, the main oxidation state of Ni in $LaNi_{0.5}Ti_{0.5}O_3$ is Ni^{2+}. The corresponding O 1s spectrum features a peak at 530.0 eV (lattice oxygen of the perovskite structure) with a high-binding energy shoulder at 531.8 eV (surface-related oxygen species) [51,52]. Any reductive treatment (either directly in the DRM mixture or in hydrogen) causes a distinct response both in the Ti 2p and O 1s spectra by featuring a more reduced component. For Ti 2p, a doublet for Ti^{3+} arises at 457.3 eV and 463.0 eV, which is most prominent after a hydrogen pre-treatment. Also observed after one DRM cycle, it gets more pronounced after a second DRM cycle due to the higher amount of exsolved Ni. The corresponding O 1s spectra all feature a small component at 528.7 eV, attributed to surface oxidation of exsolved Ni particles. We assume NiO arises by formation of a thin NiO layer upon contact to air (PXRD only show metallic Ni in the bulk). Accordingly, the lattice O 1s component decreases and the O 1s feature of NiO increases after reduction, mimicking the trend of Ti 2p as a function of reduction strength. Peculiar is the total decrease in intensity of especially the O 1s region after a hydrogen reduction – DRM cycle: according to Fig. S8, this is due the formation of a shielding graphite layer manifesting itself via a strong C 1s component at 284.4 eV. After neither of the other treatments carbon formation (i.e., coking) is observed.

3.4. Methane dry reforming performance of different Ni - lanthanum nickel titanium interfaces

Fig. 10 highlights the DRM profiles of the Ni-perovskite interfaces characterized in the preceding sections. According pre-treatments have been conducted to induce the formation of the discussed Ni-perovskite interfaces. To illustrate the influence of Ti, we have also added the

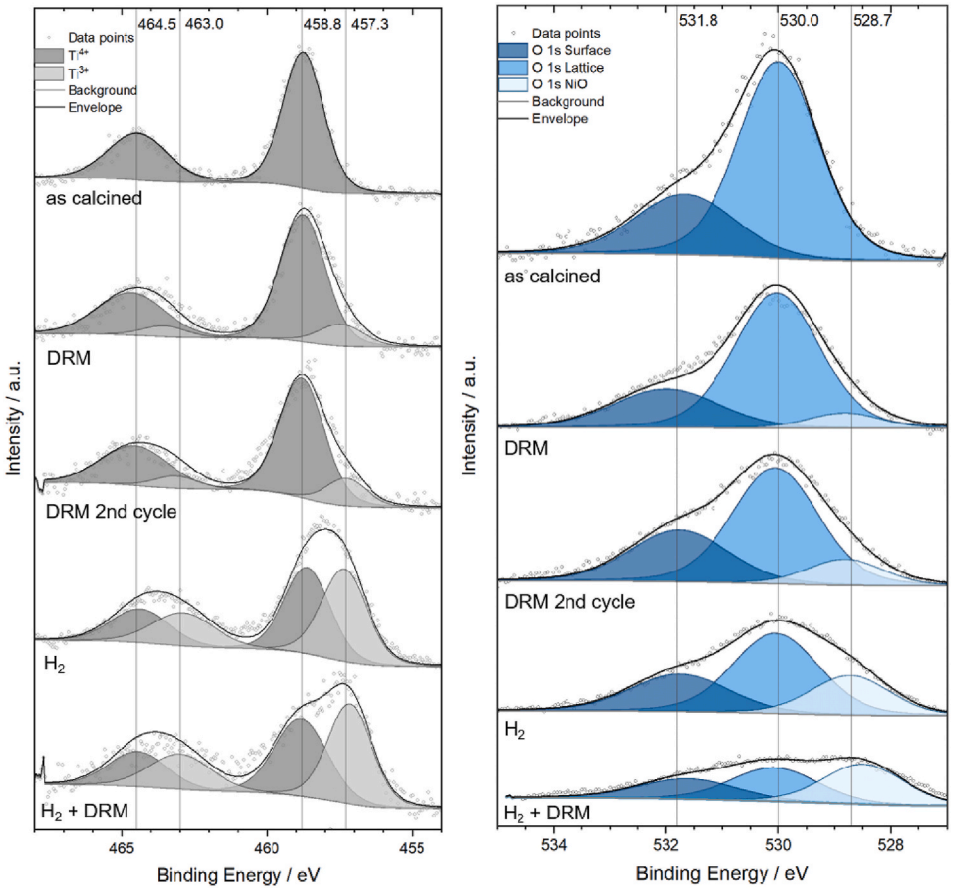

Fig. 9. High-resolution Ti 2p (left) and O 1s XP spectra (right) measured on $LaNi_{0.5}Ti_{0.5}O_3$ after selected treatments as indicated.

DRM profile of $LaNiO_3$ after hydrogen pre-reduction. At first glance, all Ni-perovskite interfaces exhibit DRM activity. Ni in contact with La_2TiNiO_6 (top left) features the worst behaviour with a reaction onset at ca. 500 °C and final conversions of 80 % (for CO_2) and ca. 65 % (for CH_4). The higher conversion of CO_2 (which translates into a H_2/CO ratio of about 0.8) indicates concurrent reverse water-gas shift activity as a common feature on many perovskites during DRM [53–56]. For $LaNi_{0.5}Ti_{0.5}O_3$, where Ni exsolution is much more pronounced even without hydrogen pre-treatment, we observe a distinct induction period of metallic Ni exsolution during the first DRM cycle (dashed profiles, top left). A sharp increase in the DRM activity at 750 °C indicates reduction of oxidized Ni to metallic Ni. After Ni activation, the DRM activity is stable. A second DRM cycle, which now reflects the inherent activity of the Ni–$LaNi_{0.5}Ti_{0.5}O_3$ interface, features a light-off temperature of around 425 °C and conversions of 98 % (CO_2) and 92 % (CH_4). Whereas a H_2/CO ratio of almost unity is observed during the isothermal period in the first cycle (where the activity is, hence, dominated by metallic Ni with exclusive DRM activity), the H_2/CO ratio drops to around 0.93 in the second cycle, respectively. This indicates a modest contribution of the reverse water-gas shift reaction on the perovskite. Referenced to the activity of $LaNiO_3$, we note that the reaction onset for $LaNiO_3$ is slightly lower (around 350 °C), but the overall reaction profile for the latter is much more complex due to the efficient structural decomposition of $LaNiO_3$. If a pre-reduction in hydrogen (1000 °C, 1 h) is carried out before DRM (bottom left) to induce the Ni exsolution (equivalent to the total decomposition of $LaNi_{0.5}Ti_{0.5}O_3$), the onset temperature of catalytic activity is lowered to ca. 380 °C. We note that XPS showed a large graphitic carbon content on the surface (cf. Fig. S8) after this hydrogen-DRM cycle.

Compared to $LaNiO_3$, hydrogen reduction of $LaNi_{0.5}Ti_{0.5}O_3$ removes the activity decrease of the former between 650 °C and 750 °C. This "bump" in activity often occurs during DRM on perovskites and arises from competing reactions of the DRM network on transient species [57–59]. Doping with Ti not only stabilizes the entire perovskite structurally, but this, in turn, has a beneficial effect on the high-temperature DRM activity. As indicated in Table S2, comparing the activity of different Ni perovskite samples, as well as Ni on Al_2O_3, $LaNi_{0.5}Ti_{0.5}O_3$ after hydrogen reduction, despite the structural complexity, outperforms most of the materials in terms of activity under comparable experimental conditions.

With respect to the reaction mechanism, we note that for $LaNiO_3$, the carbon dioxide activation via reversible carbonization of La_2O_3 to $La_2O_2CO_3$ is in the epicentre of catalytic activity. In all $LaNiO_3$ and Cu-doped La_2NiO_4 phases, crystalline monoclinic $La_2O_2CO_3$ was detected during peak activity and in the spent catalyst state [6,7]. On the contrary, for none of the Ti-doped $LaNiO_3$ phases we detected any activated crystalline carbon species resulting from carbon dioxide decomposition – most likely, because no La_2O_3 was observed, even for fully decomposed $LaNi_{0.5}Ti_{0.5}O_3$. Several studies have suspected, that the role of the (oxygen-deficient) perovskite is to aid the carbon dioxide activation and to provide oxygen spillover to Ni to enhance the removal of surface carbon deposits [4]. As our studies do reveal only a minor (if any) presence of reduced sites in either studied perovskite sample, we suggest that the dry reforming activity for the Ti-doped $LaNiO_3$ phases is driven by the activation properties of Ni alone, and the role of the perovskite in essence is to stabilize active Ni particle sizes. This is also confirmed by additional experiments on the corresponding Ni-free $La_2Ti_2O_7$ phase. The latter is the stable Ni-free end composition in the La–Ti–Ni–O phase diagram at room temperature. The corresponding $LaTiO_3$ perovskite exists, but is usually prepared by arc-melting [60]. As shown in Fig. S9, $La_2Ti_2O_7$ is DRM inactive.

The hypothesis of a stabilizing role of these perovskites is also

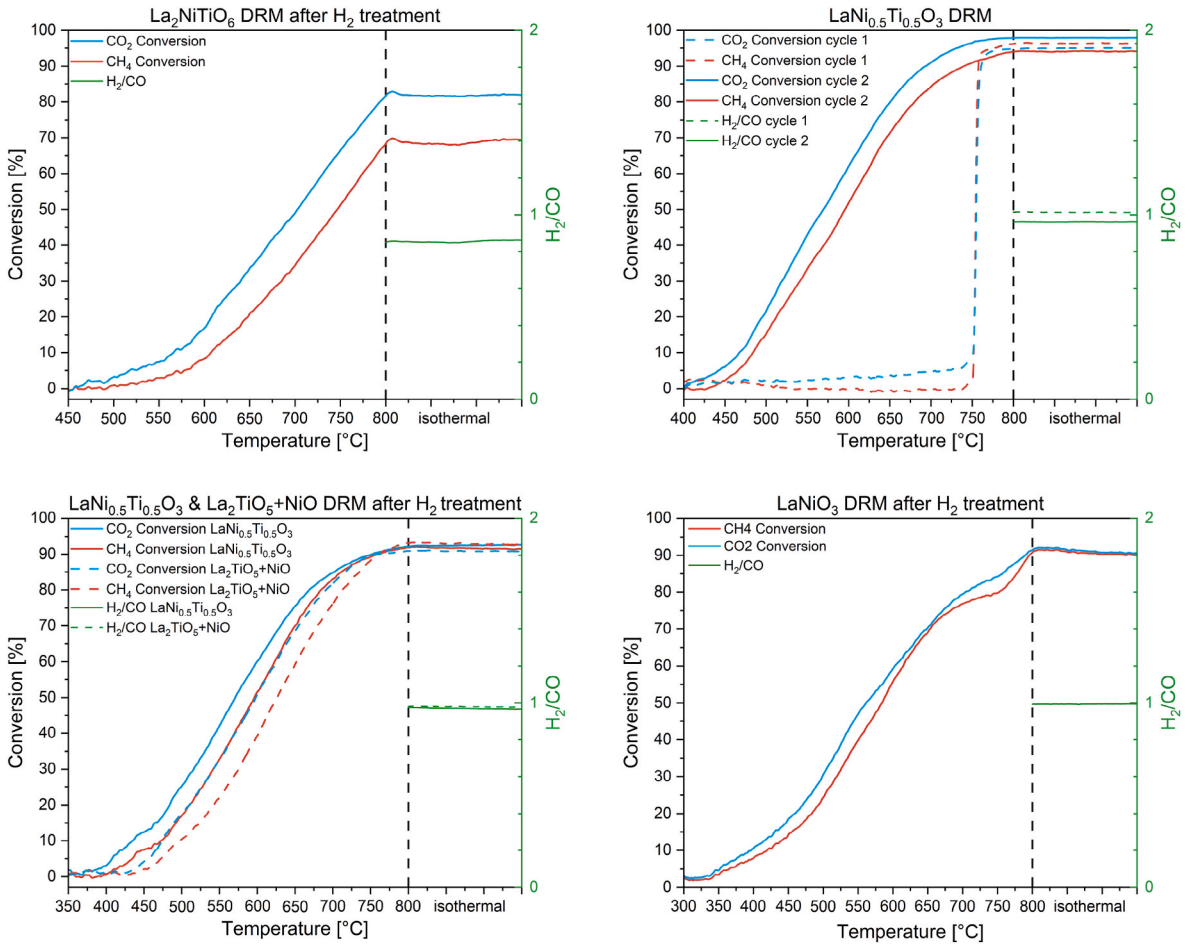

Fig. 10. Methane dry reforming profiles of La_2TiNiO_6 and $LaNi_{0.5}Ti_{0.5}O_3$ after selected reductive pre-treatments. *Top left*: DRM experiment on La_2TiNiO_6 after a hydrogen pre-treatment at 1000 °C for 1 h. *Top right*: $LaNi_{0.5}Ti_{0.5}O_3$ without hydrogen pre-treatment. *Bottom left*: DRM experiments on $LaNi_{0.5}Ti_{0.5}O_3$ after a hydrogen pre-treatment at 1000 °C for 1 h (solid traces), in comparison to wet-impregnated Ni particles on La_2TiO_5 after hydrogen reduction at 800 °C for 15 min (broken traces). *Bottom right*: DRM experiment on $LaNiO_3$ after a hydrogen pre-treatment at 1000 °C for 1 h. Green profiles denote the H_2/CO ratios. Heating rate: 5 °C min^{-1}, sample mass: 200 mg each, gas flow: CO_2:CH_4:He = 20 mL:20 mL:20 mL, GHSV: 18 $Lh^{-1}g_{cat}^{-1}$.

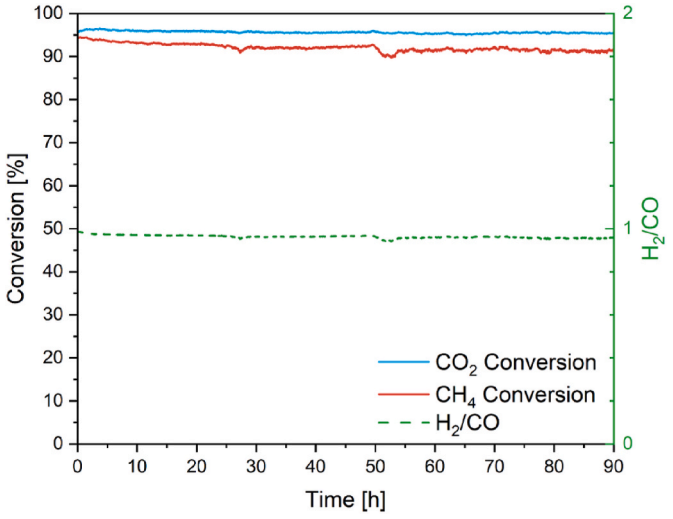

Fig. 11. DRM profile of an 90 h time-on-stream experiment at 800 °C on $LaNi_{0.5}Ti_{0.5}O_3$ after prior 1 h reduction in H_2 at 1000 °C. The green profile denotes the H_2/CO ratio. Sample mass: 200 mg, gas flow: CO_2:CH_4:He = 20 mL:20 mL:20 mL, GHSV: 18 $Lh^{-1}g_{cat}^{-1}$.

corroborated by the highest activity of Ni in contact with La_2TiO_5 and $LaTiO_3$. In this respect, the carbon dioxide activation properties of Ni have recently been shown to strongly depend on the Ni particle size and the nature of the oxide to which Ni is anchored to [61]. The catalytic role of the perovskite for $LaNi_xTi_{1-x}O_3$ in fact appears to be to merely catalyze selectively-spoiling reactions: in this particular case, e.g., by contributing reverse water-gas shift activity for $LaNi_{0.5}Ti_{0.5}O_3$ directly activated during DRM.

To determine the long-term stability of the best working catalyst, i.e., $LaNi_{0.5}Ti_{0.5}O_3$ after hydrogen reduction at 1000 °C and subsequent DRM, representing Ni particles in contact with La_2TiO_5 and $LaTiO_3$, Fig. 11 shows the DRM profiles of this catalyst over a period of 90 h time-on-stream at 800 °C. Conversions of carbon dioxide and methane remain stable throughout the duration of the experiment at 95 % and 92 %, respectively. The H_2/CO ratio remains close to unity, indicating stable DRM performance. Catalytic-site wise, two experimental results of spent catalyst characterization provide further insight: At first, ex-situ XRD of the sample after the experiment reveals that most of the $LaTiO_3$ has transformed into La_2TiO_5 during the long-term measurement (a drop from 25 wt.-% after 1 h time-on-stream to ca. 2 wt% after 90 h has been observed for $LaTiO_3$, accompanied by an increase of La_2TiO_5 from 56 wt % to 72 wt%; see Table 1 and Fig. S9). This strongly suggests, that even in the beginning of the experiment, and more true so for the long-term measurement, the Ni–La_2TiO_5 interface is important for catalytic activity. To prove this point, we have synthesized a Ni–La_2TiO_5 interface

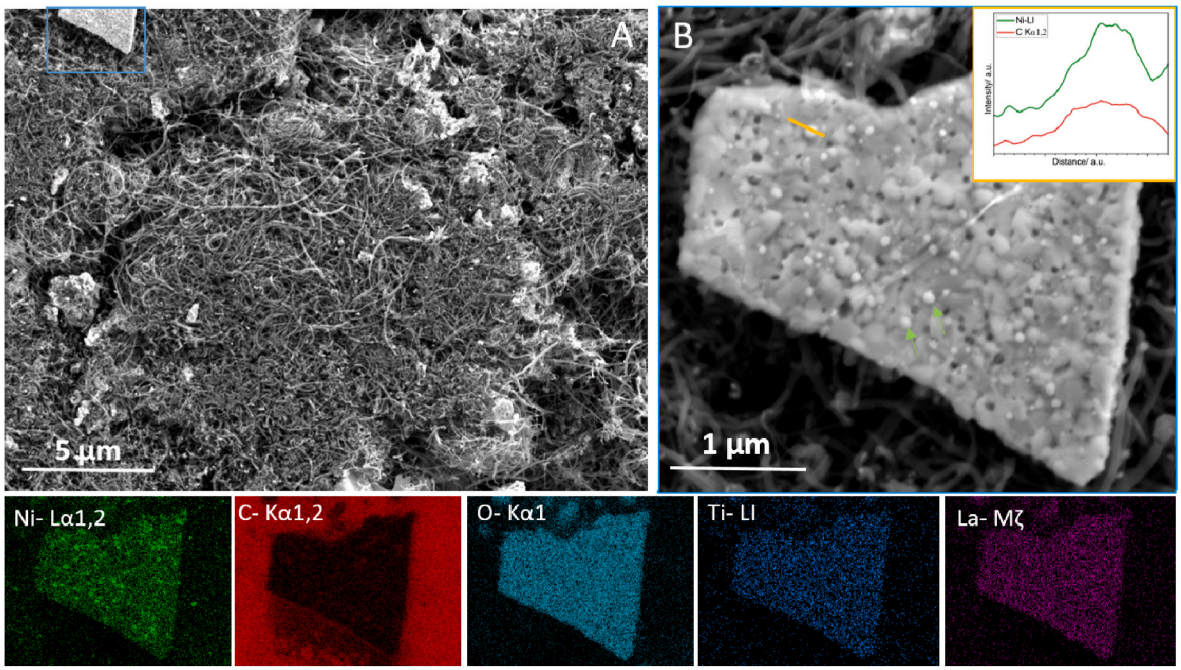

Fig. 12. SEM/EDX characterization of the spent catalyst state of $LaNi_{0.5}Ti_{0.5}O_3$ after hydrogen reduction at 1000 °C followed by DRM at 800 °C for 90 h time-on-stream. Panel A: Overview image. Panel B: Image of an un-coked La_2TiO_5 region with Ni particles without carbon fibre formation. The orange line shows the region where the line scan (upper right corner) was performed. The two green arrows denote the location of two Ni particles. Bottom row: Individual EDX maps of Ni (green), C (red), O (turquoise), Ti (blue) and La (magenta).

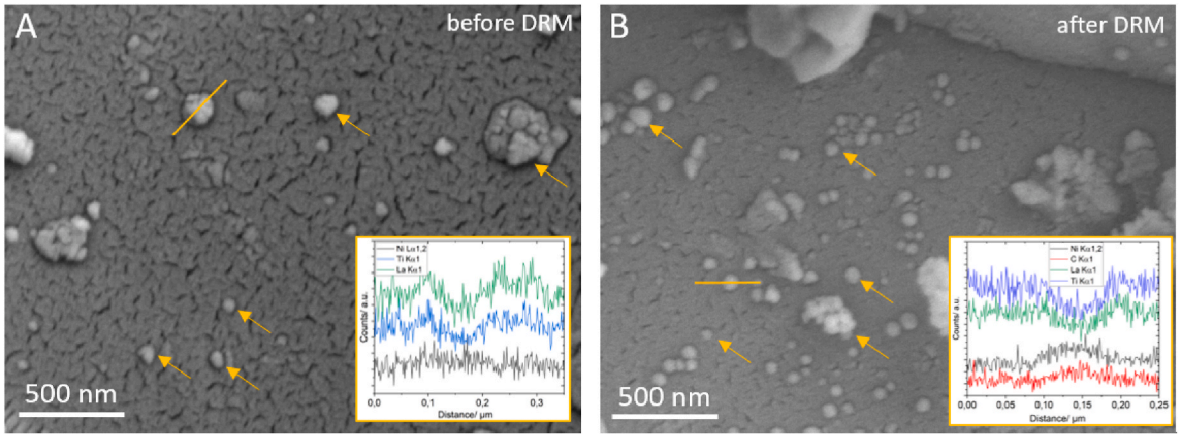

Fig. 13. SEM/EDX characterization of wet-impregnated Ni/La_2TiO_5 before (Panel A) and after a hydrogen pre-reduction - DRM (Panel B). The insets show representative EDX line profiles to locate Ni particles. The porous background structure stems from the 20 nm thick Au coating layer to prevent charging. Several Ni particles are marked by arrows. Experimental conditions as in Fig. 10.

by wet-impregnation and accordingly tested it in DRM (Fig. 10, bottom left Panel, broken traces). Evidently, the overall shape of the DRM profile is very similar, with only a minor difference in catalytic onset temperature (pure La_2TiO_5 without Ni is also DRM-inactive). Secondly, XP spectra, SEM images and PXRD patterns (Figs. 9 and 12, Figs. S10–S12) all reveal a rather strong graphitic carbon accumulation by mostly filament formation both after 1 h and 90 h time-on-stream. Interestingly, this is not detrimental to catalytic activity. SEM images after 90 h time-on-stream show that although massive carbon fibre formation is visible, extended patches of La_2TiO_5 (which is the dominant phase according to XRD) with small Ni particles without filament formation are frequently visible (one is marked by a blue rectangle in Fig. 12, Panel A and shown as close-up in Panel B with the respective EDX maps). This implies that La_2TiO_5 is able to stabilize a critical Ni particle size, which is resistant to fibre formation. The line scan (orange, inset in Panel B) shows a carbon signal located at the Ni particles – we assume that this reflects a small amount of dissolved carbon within the bulk of the fibre-free Ni particles. A graphite-like coating layer is excluded based on the highly stable DRM activity over 90 h time-on-stream. We have validated the improved anti-coking behavior of Ni/La_2TiO_5 by performing XRD and SEM analysis of the impregnated Ni/La_2TiO_5 material before and after the reduction-DRM cycling: no sintering of Ni particles occurs and coking is essentially suppressed on Ni/La_2TiO_5 (Fig. 13 and S13).

4. Conclusions

We have shown that the lanthanum-nickel-titanate system offers a perfect opportunity to access the inherent reactivity of different metal-perovskite interfaces in DRM. Summarized as bullet points, the main

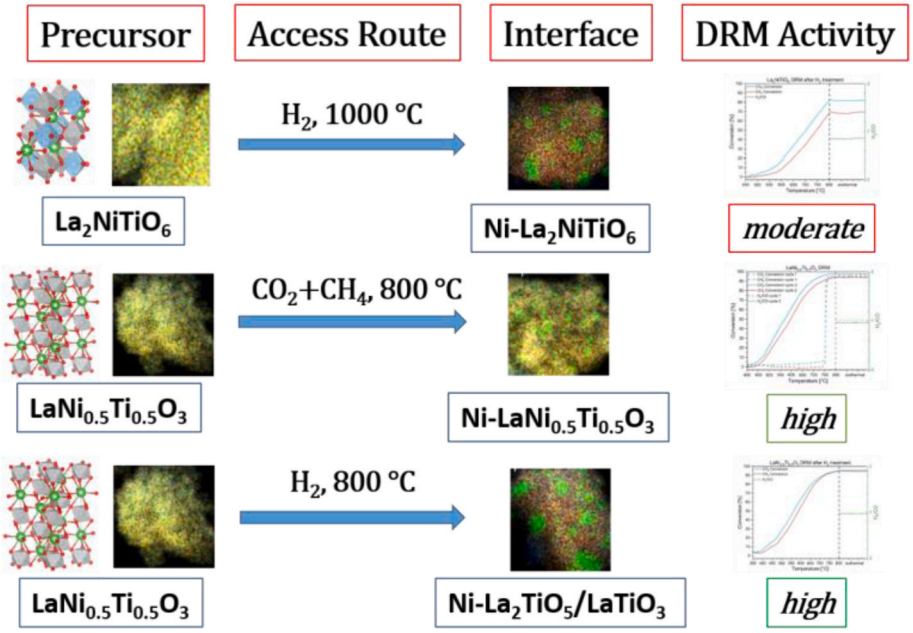

Scheme 1. Overview of the precursors, access routes, interfaces and connected DRM activity.

conclusions are.

- *Strategies to access well-defined metal-perovskite interfaces*: In most of the literature-discussed perovskites over all catalytic applications, little care is taken to ensure that the Ni-perovskite interfaces are well-defined in terms of structure, phase and elemental composition. Exploiting the enhanced structural stability of different Ti-doped $LaNiO_3$ perovskites, i.e., the double perovskite La_2NiTiO_6 and the single perovskite $LaNi_{0.5}Ti_{0.5}O_3$, in different reducing atmospheres allowed us to disentangle the inherent DRM reactivity of Ni in contact with either La_2NiTiO_6 or $LaNi_{0.5}Ti_{0.5}O_3$ and to benchmark this reactivity against undoped $LaNiO_3$, $La_2Ti_2O_7$ and Ni in contact with a fully decomposed perovskite precursor. Careful selection of the reduction potential of the gas atmosphere is the key parameter for the successful synthesis of different Ni-perovskite interfaces.
- *Consequences for inherent DRM activity of the specific Ni-provskite interfaces*: Both Ni–La_2TiNiO_6 and Ni–$LaNi_{0.5}Ti_{0.5}O_3$ are structure- and phase-stable over several DRM cycles and the latter is also long-term stable over extended time-on-stream periods, rivaling or even outperforming undoped $LaNiO_3$.
- *The specific role of Ti as a structure-stabilizing dopant*: Ti stabilizes the parent $LaNiO_3$ structure in reducing atmospheres by enabling a Ti^{4+}/Ti^{3+} redox couple, thereby largely suppressing the formation of reduced sites. In due course, intermediate structures and phases, such as La_2NiO_4, are also stabilized along the exsolution and decomposition pathway. Doping of $LaNiO_3$ with Ti is the crucial factor to suppress perovskite decomposition and to accordingly access specific Ni-perovskite interfaces.
- *Effect of Ti on the reaction mechanism in DRM*: Contrary to the usual role ascribed to the perovskite for a metal-perovskite interface, the impact of reduced sites seems to be suppressed in the $LaNi_xTi_{1-x}O_3$ system. The inherent detrimental contribution of the perovskite is the selectivity-spoiling reverse water-gas shift reaction. Beneficially, catalytically active Ni particle sizes are apparently stabilized at the Ni-perovskite interface. The DRM reaction mechanism on $LaNiO_3$ via a reversible La oxycarbonate CO_2 activation cycle is at least suppressed for La_2TiNiO_6 and $LaNi_{0.5}Ti_{0.5}O_3$ due to i) the stabilizing effect of Ti suppressing the formation of La_2O_3 necessary for the formation of lanthanum oxycarbonate, and ii) the reaction of Ti with La to form ternary oxides with higher stability.
- *The role of La_2TiO_5 for catalytic activity*: La_2TiO_5 as the dominant lanthanum-titanium phase in the best-performing catalyst stabilizes a critical Ni particle size with improved coking resistance. The beneficial role of La_2TiO_5 for suppressing coke formation on Ni-containing catalyst materials in reforming reactions seems to be universal, as also for methane steam reforming, this pivotal role has been pointed out [32].

Scheme 1 gives a summarizing overview of the structures and catalytic activity of the different Ni-perovskite interfaces.

With $LaNi_xTi_{1-x}O_3$ we provide model system that allows to emphasize the importance of well-defined metal-perovskite interfaces to understand their inherent catalytic properties. Across many catalytic applications, due to the strategy of exsolution of metal particles from a perovskite host lattice, the formation of a metal-perovskite interface is a frequently observed phenomenon. In due course, a bifunctional synergistic reaction mechanism usually prevails - either by a direct contribution with inherent catalytic activity of the individual catalyst entities or indirectly by structural stabilization effects. Notwithstanding their exact catalytic role, the presence of well-defined metal-perovskite interfaces is imperative to disentangle the individual roles and to determine the inherent interfacial activity.

CRediT authorship contribution statement

Thomas F. Winterstein: Methodology, Investigation, Formal analysis, Data curation. **Christoph Malleier:** Methodology, Investigation, Formal analysis, Data curation. **Asghar Mohammadi:** Methodology, Investigation, Formal analysis, Data curation. **Hannes Krüger:** Methodology, Investigation, Formal analysis, Data curation. **Volker Kahlenberg:** Writing – review & editing, Supervision, Formal analysis, Conceptualization. **Andrew M. Venter:** Methodology, Investigation, Formal analysis, Data curation. **Maged F. Bekheet:** Writing – review & editing, Supervision, Formal analysis, Conceptualization. **Julian T. Müller:** Writing – review & editing, Data curation. **Aleksander Gurlo:** Writing – review & editing. **Marc Heggen:** Writing – review & editing, Formal analysis, Data curation. **Simon Penner:** Writing – review & editing, Writing – original draft, Validation, Supervision, Project administration, Funding acquisition, Conceptualization.

Declaration of competing interest

The authors declare the following financial interests/personal relationships which may be considered as potential competing interests: Simon Penner reports financial support was provided by FWF. If there are other authors, they declare that they have no known competing financial interests or personal relationships that could have appeared to influence the work reported in this paper.

Acknowledgments

The work was conducted within the framework of the Research Focus "Functional Materials" at the University of Innsbruck. This research was funded in whole by the Austrian Science Fund (FWF) 10.55776/P35770. For open access purposes, the author has applied a CC BY public copyright license to any author accepted manuscript version arising from this submission. The authors thank the Advanced Light Source, which is supported by the Director, Office of Science, Office of Basic Energy Sciences, of the U.S. Department of Energy under Contract No. DE-AC02- 05CH11231, and where the in situ XRD measurements were conducted at beamline 12.2.2 in the framework of the AP proposals (ALS-11921). We thank Dr. Julian Hungerford from Micromeritics for assistance with the BET measurements.

Appendix A. Supplementary data

Supplementary data to this article can be found online at https://doi.org/10.1016/j.mtchem.2025.102620.

Data availability

Raw data of measurement files can be accessed via a repository for research data at the University of Innsbruck using the doi link 10.48323/krjst-dn721.

References

[1] N. Aramouni, J. Touma, B. Tarboush, J. Zeaiter, M. Ahmad, Catalyst design for dry reforming of methane: analysis review, Renew. Sustain. Energy Rev. 82 (2018) 2570–2585, https://doi.org/10.1016/j.rser.2017.09.076.

[2] S. Bhattar, M. Abedin, S. Kanitkar, J. Spivey, A review on dry reforming of methane over perovskite-derived catalysts, Catal. Today 365 (2021) 2–23, https://doi.org/10.1016/j.cattod.2020.10.041.

[3] W. Jang, J. Shim, H. Kim, S. Yoo, H. Roh, A review on dry reforming of methane in aspect of catalytic properties, Catal. Today 324 (2019) 15–26, https://doi.org/10.1016/j.cattod.2018.07.032.

[4] S. Vasala, M. Karppinen, $A_2B'B''O_6$ perovskites: a review, Prog. Solid State Chem. 43 (2015) 1–36, https://doi.org/10.1016/j.progsolidstchem.2014.08.001.

[5] X. Xu, Y. Zhong, Z. Shao, Double perovskites in catalysis, electrocatalysis and photo (electro)catalysis, Trends in Chemistry 1 (2019) 410–424, https://doi.org/10.1016/j.trechem.2019.05.006.

[6] N. Bonmassar, M.F. Bekheet, L. Schlicker, A. Gili, A. Gurlo, A. Doran, Y. Gao, M. Heggen, J. Bernardi, B. Klötzer, S. Penner, In situ-determined catalytically active state of $LaNiO_3$ in methane dry reforming, ACS Catal. 10 (2020) 1102–1112, https://doi.org/10.1021/acscatal.9b03687.

[7] M.F. Bekheet, et al., Steering the methane dry reforming reactivity of Ni/La_2O_3 catalysts by controlled in situ decomposition of doped La_2NiO_4 precursor structures, ACS Catal. 11 (2021) 43–59, https://doi.org/10.1021/acscatal.0c04290.

[8] S.A. Malyshev, O.A. Shlyahktin, S. Huang, G.M. Timofeev, G.N. Mazo, I. V. Roslyakov, A.V. Vasiliev, A.L. Kustov, Metal-oxide nanocomposites by low temperature exsolution from perovskite-like La nickelates: synthesis, morphology, and catalytic properties in CO2 hydrogenation, Mater. Res. Bull. 179 (2024) 112984, https://doi.org/10.1016/j.materresbull.2024.112984.

[9] C. Malleier, S. Penner, Metal-perovskite interfacial engineering to boost activity in heterogeneous catalysis, Surfaces 7 (2024) 296–339, https://doi.org/10.3390/surfaces7020020.

[10] T. Hayakawa, S. Suzuki, J. Nakamura, T. Uchijima, S. Hamakawa, K. Suzuki, T. Shishido, K. Takehira, CO_2 reforming of CH_4 over Ni/perovskite catalysts prepared by solid phase crystallization method, Appl. Catal. A 183 (1999) 273–285, https://doi.org/10.1016/S0926-860X(99)00071-X.

[11] S. Joo, A. Seong, O. Kwon, K. Kim, J.H. Lee, R.J. Gorte, J.M. Vohs, J.W. Han, J. W. G, Highly active dry methane re-forming catalysts with boosted in situ grown Ni-Fe nanoparticles on perovskite via atomic layer deposition, Sci. Adv. 6 (2020) 2375–2548, https://doi.org/10.1126/sciadv.abb1573.

[12] S. Dama, S. Ghudke, R. Bobade, H. Gurav, S. Chilukuri, Tuning the dimensionality of layered $Sr_{n+1}Ti_{n-x}Ni_xO_{3n+1}$ perovskite structures for improved activity in syngas generation, J. Catal. 360 (2018) 27–39, https://doi.org/10.1016/j.jcat.2018.01.015.

[13] S. Nuvula, T.V. Sagar, D. Valluri, P. Prasad, Selective substitution of Ni by Ti in $LaNiO_3$ perovskites: a parameter governing the oxy-carbon dioxide reforming of methane, Int. J. Hydrogen Energy 43 (2018) 4136–4142, https://doi.org/10.1016/j.ijhydene.2017.08.180.

[14] S. Lou, X. Meng, N. Liu, L. Shi, A-site deficient titanate perovskite surface with exsolved nickel nanoparticles for ethanol steam reforming, Chem. Eng. Sci. 274 (2023) 118690, https://doi.org/10.1016/j.ces.2023.118690.

[15] M.M. Vijatovic, J.D. Bobic, B.D. Stojanovic, History and challenges of barium titanate: part I, Sci. Sinter. 40 (2008) 155–165, https://doi.org/10.2298/SOS0802155V.

[16] V. Grover, B.P. Mandal, A.K. Tyagi, Solid state synthesis of materials, in: A. K. Tyagi, R.S. Ningthoujam (Eds.), Handbook on Synthesis Strategies for Advanced Materials, Indian Institute of Metals Series. Springer, Singapore, 2021, https://doi.org/10.1007/978-981-16-1807-9_1.

[17] A. Doran, L. Schlicker, C. Beavers, S. Bhat, M.F. Bekheet, A. Gurlo, Compact low power infrared tube furnace for in situ X-ray powder diffraction, Rev. Sci. Instrum. 88 (2017) 013903, https://doi.org/10.1063/1.4973561.

[18] L. Schlicker, A. Doran, P. Schneppmüller, A. Gili, M. Czasny, S. Penner, A. Gurlo, Transmission in situ and operando high temperature X-ray powder diffraction in variable gaseous environments, Rev. Sci. Instrum. 89 (2018) 033904, https://doi.org/10.1063/1.5001695.

[19] DIFFRAC, TOPAS 5.0, Bruker (2024).

[20] A. Mohammadi, A. Farzi, C. Thurner, B. Klötzer, S. Schwarz, J. Bernardi, A. Niaei, S. Penner, Tailoring the metal-perovskite interface for promotional steering of the catalytic NO reduction by CO in the presence of H_2O on Pd-lanthanum iron manganite composites, Appl. Catal., B 307 (2022) 121160, https://doi.org/10.1016/j.apcatb.2022.121160.

[21] M. Grünbacher, E. M. Köck, M. Kogler, B. Klötzer, S. Penner, Evidence for dissolved hydrogen in the mixed ionic–electronic conducting perovskites $La_{0.6}Sr_{0.4}FeO_{3-\delta}$ and $SrTi_{0.7}Fe_{0.3}O_{3-\delta}$, Phys. Chem. Chem. Phys. 18 (2016) 26873-26884, DOI 10.1039/C6CP05392K.

[22] A.M. Venter, P.R. van Heerden, D. Marais, J.C. Raaths, Z.N. Sentsho, PITSI: the neutron powder diffractometer for transition in structure investigations at the SAFARI-1 research reactor, Phys. B 551 (2018) 422–425, https://doi.org/10.1016/j.physb.2017.12.017.

[23] Bruker, TOPAS (Version 6.0), Bruker AXS, Karlsruhe Germany, 2016.

[24] E. Momma, F. Izumi, VESTA 3 for three-dimensional visualization of crystal, volumetric and morphology data, J. Appl. Cryst. 44 (2011) 1272–1276, https://doi.org/10.1107/S0021889811038970.

[25] E. Rodriguez, M.L. López, J. Campo, M.L. Veiga, C. Pico, Crystal and magnetic structure of the perovskites La_2MTiO_6 (M = Co, Ni), J. Mater. Chem. 12 (2002) 2798–2802, https://doi.org/10.1039/B202504N.

[26] V.F. Sears, Neutron scattering lengths and cross sections, Neutron News 3 (1992) 26–37.

[27] J.L. Garcia-Munoz, J. Rodriguez-Carvajal, P. Lacorre, J.B. Torrance, Neutron-diffraction study of $RNiO_3$ (R=La,Pr,Nd,Sm): electronically induced structural changes across the metal-insulator transition, Phys. Rev. B 46 (1992) 4414, https://doi.org/10.1103/PhysRevB.46.4414.

[28] J.O. Conway, T.J. Prior, Interstitial nitrides revisited – a simple synthesis of M_xMo_3N (M = Fe, Co, Ni), J. Alloys Compd. 74 (2019) 69–74, https://doi.org/10.1016/j.jallcom.2018.09.307.

[29] R.D. Aughterson, G.R. Lumpkin, G.J. Thorogood, Z. Zhang, B. Gault, J.M. Cairney, Crystal chemistry of the orthorhombic Ln_2TiO_5 compounds with Ln=La, Pr, Nd, Sm, Gd, Tb and Dy, J. Solid State Chem. 227 (2015) 60–67, https://doi.org/10.1016/j.jssc.2015.03.003.

[30] M. Cwik, T. Lorenz, J. Baier, R. Müller, G. Andre, F. Bouree, F. Lichtenberg, A. Freimuth, R. Schmitz, E. Müller-Hartmann, M. Braden, Crystal and magnetic structure of $LaTiO_3$: evidence for nondegenerate *t2g* orbitals, Phys. Rev. B 68 (2003) 060401, https://doi.org/10.1103/PhysRevB.68.060401.

[31] J. Rodriguez-Carvajal, M.T. Fernandez-Diaz, J.L. Martinez, Neutron diffraction study on structural and magnetic properties of La_2NiO_4, J. Phys. Condens. Matter 3 (1991) 3215, https://doi.org/10.1088/0953-8984/3/19/002.

[32] P.V. Tuza, M. Souza, Steam reforming of methane over catalyst derived from ordered double perovskite: effect of crystalline phase transformation, Catal. Lett. 146 (2016) 47–53, https://doi.org/10.1007/s10562-015-1617-1.

[33] C. Arrive, T. Delahaye, O. Joubert, G. Gauthier, Exsolution of nickel nanoparticles at the surface of a conducting titanate as potential hydrogen electrode material for solid oxide electrochemical cells, J. Power Sources 223 (2013) 341–348, https://doi.org/10.1016/j.jpowsour.2012.09.062.

[34] Y. Cui, V. Galvita, L. Rihko-Struckmann, H. Lorenz, K. Sundmacher, Steam reforming of glycerol: the experimental activity of $La_{1-x}Ce_xNiO_3$ catalyst in comparison to the thermodynamic reaction equilibrium, App, Catal. B. 90 (2009) 29–37, https://doi.org/10.1016/j.apcatb.2009.02.006.

[35] S. Ramesh, N. Venkatesha, Template free synthesis of Ni-perovskite: an efficient catalyst for hydrogen production by steam reforming of bioglycerol, ACS Sustain. Chem. Eng. 5 (2017) 1339–1346, https://doi.org/10.1021/acssuschemeng.6b01744.

[36] G. Valderrama, M.R. Goldwasser, C.U. de Navarro, J.M. Tatibouët, J. Barrault, C. Batiot-Dupeyrat, F. Martínez, Dry reforming of methane over Ni perovskite type oxides, Catal. Today 107 (2005) 785–791, https://doi.org/10.1016/j.cattod.2005.07.010.

[37] J.Y. Liu, W.N. Su, J. Rick, S.C. Yang, J.H. Cheng, C.J. Pan, J.F. Lee, B.J. Hwang, Hierarchical copper-decorated nickel nanocatalysts supported on La_2O_3 for low-temperature steam reforming of ethanol, ChemSusChem 77 (2014) 570–576, https://doi.org/10.1002/cssc.201300737.
[38] M. Rivas, J. Fierro, R. Guil-Lopez, M. Pena, V. La Parola, M. Goldwasser, Preparation and characterization of nickel-based mixed-oxides and their performance for catalytic methane decomposition, Catal. Today 133 (2008) 367–373, https://doi.org/10.1016/j.cattod.2007.12.045.
[39] P. Levitz, M. Crespin, L. Gatineau, Reduced forms of $LaNiO_3$ perovskite. Part 1.—evidence for new phases: $La_2Ni_2O_5$ and $LaNiO_2$, J. Chem. Soc., Faraday Trans. 79 (1983) 1181–1194, https://doi.org/10.1039/F29837901181.
[40] T. Nakamura, G. Petzow, L. Gauckler, Stability of the perovskite phase $LaBO_3$ (B= V, Cr, Mn, Fe, Co, Ni) in reducing atmosphere I. Experimental results, Mater. Res. Bull. 14 (1979) 649–659, https://doi.org/10.1016/0025-5408(79)90048-5.
[41] A. Ruiz Puigdollers, P. Schlexer, S. Tosoni, G. Pacchioni, Increasing oxide reducibility: the role of metal/oxide interfaces in the formation of oxygen vacancies, ACS Catal. 7 (2017) 6493–6513, https://doi.org/10.1021/acscatal.7b01913.
[42] A. Mohammadi, et al., Copper-perovskite interfacial engineering to boost deNO_x activity, Chem. Eng. J. 498 (2024) 155425, https://doi.org/10.1016/j.cej.2024.155425.
[43] G. Wu, C. Zhang, S. Li, Z. Han, T. Wang, X. Ma, J. Gong, Hydrogen production via glycerol steam reforming over Ni/Al_2O_3: influence of nickel precursors, ACS Sust. Chem.& Eng. 1 (2013) 1052–1062, https://doi.org/10.1021/sc400123f.
[44] L. Zhang, J. Lin, Y. Chen, Characterization of dispersion and surface states of NiO/γ-alumina and NiO/La_2O_3–γ-alumina catalysts, J. Chem. Society, Faraday Trans. 88 (1992) 497–502, https://doi.org/10.1039/FT9928800497.
[45] M. Wu, D.M. Hercules, Studies of supported nickel catalysts by X-ray photoelectron and ion scattering spectroscopies, J. Phys. Chem. 83 (1979) 2003–2008, https://doi.org/10.1021/j100478a015.
[46] J.F. Moulder, W.F. Stickle, P.E. Sobol, K.D. Bomben, in: J. Chastain (Ed.), Handbook of X-Ray Photoelectron Spectroscopy, Perkin Elmer Corporation, 1992.
[47] M.C. Biesinger, B.P. Payne, B.R. Hart, A.P. Grosvenor, N.S. McIntye, L.W.M. Lau, R. St C. Smart, Quantitative chemical state XPS analysis of first row transition metals, oxides and hydroxides, J. Phys.: Conf. Ser. 100 (2008) 012025, https://doi.org/10.1088/1742-6596/100/1/012025.
[48] M.C. Biesinger, L.W.M. Laua, A.R. Gerson, R. St C. Smart, Resolving surface chemical states in XPS analysis of first row transition metals, oxides and hydroxides: Sc, Ti, V, Cu and Zn, Appl. Surf. Sci. 257 (2010) 887–898, https://doi.org/10.1016/j.apsusc.2010.10.051.
[49] M. Murata, K. Wakino, S. Ikeda, X-ray photoelectron spectroscopic study of perovskite titanates and related compounds: an example of the effect of polarization on chemical shifts, J. Electron. Spectrosc. Relat. Phenom. 6 (1975) 459, https://doi.org/10.1016/0368-2048(75)80032-6.
[50] H. Ikawa, T. Yamada, K. Kojima, S. Matsumoto, X-Ray photoelectron spectroscopy study of high- and low-temperature forms of zirconium titanate, J. Am. Ceram. Soc. 74 (1991) 1459–1462, https://doi.org/10.1111/j.1151-2916.1991.tb04131.x.
[51] R. Sanjinés, H. Tang, H. Berger, F. Gozzo, G. Margaritondo, F. Lévy, Electronic structure of anatase TiO_2 oxide, J. Appl. Phys. 75 (1994) 2945–2951, https://doi.org/10.1063/1.356190.
[52] J. Huang, Q. Hu, X. Guo, Q. Zeng, L. Wang, L. Rethinking $Co(CO_3)_{0.5}(OH)\cdot 0.11H_2O$: a new property for highly selective electrochemical reduction of carbon dioxide to methanol in aqueous solution, Green Chem. 20 (2018) 2967–2972, https://doi.org/10.1039/C7GC03744A.
[53] S. Gao, et al., Atomic layer confined vacancies for atomic-level insights into carbon dioxide electroreduction, Nature Comm 8 (2017) 14503, https://doi.org/10.1038/ncomms14503.
[54] L. Lindenthal, et al., Novel perovskite catalysts for CO_2 utilization - exsolution enhanced reverse water-gas shift activity, Appl. Catal., B 292 (2021) 120183, https://doi.org/10.1016/j.apcatb.2021.120183.
[55] F. Orsini, et al., Exsolution-enhanced reverse water-gas shift chemical looping activity of $Sr_2FeMo_{0.6}Ni_{0.4}O_{6-\delta}$ double perovskite, Chem. Eng. J. 475 (2023) 146083, https://doi.org/10.1016/j.cej.2023.146083.
[56] A. Martinez Martin, S. Saini, D. Neagu, W. Hu, I. Metcalfe, K. Kousi, Tailoring the A and B site of Fe-based perovskites for high selectivity in the reverse water-gas shift reaction, J. CO_2 Util. 83 (2024) 102784, https://doi.org/10.1016/j.jcou.2024.102784.
[57] G. Sierra Gallego, C. Batiot-Dupeyrat, J. Barrault, E. Florez, F. Mondragon, Dry reforming of methane over $LaNi_{1-y}B_yO_{3\pm\delta}$ (B = Mg, Co) perovskites used as catalyst precursor, Appl. Catal. A 334 (2008) 251–258, https://doi.org/10.1016/j.apcata.2007.10.010.
[58] T. Wei, L. Jia, J. Luo, B. Chi, J. Pu, J. Li, J. CO_2 dry reforming of CH_4 with Sr and Ni co-doped $LaCrO_3$ perovskite catalysts, Appl. Surf. Sci. 506 (2020) 144699, https://doi.org/10.1016/j.apsusc.2019.144699.
[59] P.D.K. Nezhad, et al., Mechanistic in situ insights into the formation, structural and catalytic aspects of the La_2NiO_4 intermediate phase in the dry reforming of methane over Ni-based perovskite catalysts, Appl. Catal. A 612 (2021) 117984, https://doi.org/10.1016/j.apcata.2020.117984.
[60] M. Eitel, J.E. Greedan, A high resolution neutron diffraction study of the perovskite $LaTiO_3$, J. Less-Comm. Compds. 116 (1986) 95–104, https://doi.org/10.1016/0022-5088(86)90220-1.
[61] C. Vogt, et al., Understanding carbon dioxide activation and carbon–carbon coupling over nickel, Nature Comm 10 (2019) 5330, https://doi.org/10.1038/s41467-019-12858-3.